Robust TRIA3 and QUAD4 finite elements based on the en-RZT Kinematics for the analysis of general anisotropic multilayered composite plates

ROBUST TRIA3 AND QUAD4 FINITE ELEMENTS BASED ON THE EN-RZT KINEMATICS FOR THE ANALYSIS OF GENERAL ANISOTROPIC MULTILAYERED COMPOSITE PLATES

Matteo Sorrenti[(1)]*, Marco Gherlone[(1)]

[(1)] Department of Mechanical and Aerospace Engineering – Politecnico di Torino, Corso Duca degli Abruzzi 24, 10129 Torino, Italy

Abstract *This paper presents a new set of robust finite elements for the analysis of general anisotropic multilayered composite plates. Recently, the enhanced-Refined Zigzag Theory (en-RZT) has shown its accuracy in predicting the structural response of laminated plates exhibiting a high transverse anisotropy. Moreover, the en-RZT requires only C^0-continuous shape functions to formulate accurate and efficient finite elements. This paper focuses on the formulation of three-node triangular (TRIA3) and four-node quadrilateral (QUAD4) flat finite elements based on the en-RZT kinematics. In order to eliminate the shear-locking effect that affects low-order C^0-based elements, the constrained anisoparametric interpolation strategy and an appropriate Element Shear Correction (ESC) factor are implemented at the element level. Then, the variationally consistent triangular (enRZT-T3c) and quadrilateral (enRZT-Q4c) elements are obtained and numerically assessed. A detailed analysis has been performed to evaluate the convergence behaviour of the newly formulated elements for bending and free-vibration problems. The influence of the mesh distortion, load configurations and boundary conditions are finely addressed. The provided results and comparisons with 3D models demonstrate the accuracy and robustness of enRZT-T3c and enRZT-Q4c elements for a wide variety of problems and laminate configurations, including ultra-thin arbitrarily oriented multilayered plates.*

Keywords*: finite element method, enhanced-Refined Zigzag Theory, angle-ply laminates, computational mechanics, structural analysis, transverse shear.*

DOI: 10.1007/s11029-024-10241-y

*Corresponding Author: Dr Matteo Sorrenti; ORCID ID: 0000-0003-3536-3429; email matteo.sorrenti@polito.it

1. Introduction

Multilayered composite and sandwich structures are widely used in several engineering fields, such as aerospace, marine, energy, automotive, and civil, thanks to their remarkable mechanical properties with respect to their low weight. Among these are high strength and stiffness, corrosion resistance and fatigue life. In addition, multilayered structures can be successfully used to design performant lightweight structures due to their tailorability in manufacturing processes. However, they normally exhibit a pronounced transverse shear deformability that could lead to delamination and debonding. Thus, an appropriate mechanical model is required to accurately describe their complex structural behaviour.

In the current literature, several three-dimensional approaches are available to describe the behaviour of multilayered composite and sandwich structures. For instance, Pagano [1], Noor and Burton [2] and Savoia and Reddy [3] have presented analytical solutions for the three-dimensional elasticity of some multilayered composite plates. However, these solutions are limited to particular boundary conditions (e.g. simply supported conditions), stacking sequences (e.g. cross-ply, sandwich and anti-symmetric angle-ply) and load configurations (e.g. sinusoidal pressure). A valid alternative is represented by the Finite Element Method (FEM) and solid element formulations, which are capable of representing, in an approximated way, the three-dimensional structural response but at a high computational cost.

The researchers' efforts in finding accurate and computationally affordable solutions is demonstrated by the number of structural theories developed during the last decades. The Equivalent Single Layer (ESL) theories assume a displacement field with a known distribution across the whole laminate thickness and described by a limited number of kinematic variables independent of the lamination scheme. ESL models include the Classical Laminate Theory (CLT), the First-order Shear Deformation Theory (FSDT), Reddy's Third-order Shear Deformation Theory (TSDT), the higher-order polynomial and non-polynomial theories. The interested reader is referred to the work by Abrate and Di Sciuva [4,5] for a more detailed overview. The advantages of these models are their accuracy in predicting the global quantities of multilayered composite and sandwich structures (such as maximum deflection, frequencies and buckling loads), requiring a low computational cost. However, their predictions for the through-the-thickness distribution of in-plane displacements, strains and stresses are quite poor for moderately thick and thick laminates. In such cases, the Layer-Wise (LW) models [6] are more accurate since they assume an independent displacement field for each lamina. These theories can describe the typical displacement behaviour of laminate structures, and the strain/stress predictions are comparable to the three-dimensional solutions. The computational cost required to achieve a solution for laminates with several layers becomes prohibitive for engineering applications. In this context, the

recently developed ZigZag Theories (ZZTs) provide an alternative in the framework of the structural modelling capable of reconstructing the behaviour of multilayered structures. The displacement field is generally assumed to be the superposition of two main contributions: the global one, which can describe the general behaviour of the laminate, and the local, which is a local through-the-thickness refinement given by appropriate zigzag functions. This approach requires a limited and fixed number of variables, such as in the ESL models, but, thanks to the zigzag functions, it can reproduce the typical layerwise displacement distribution of laminated structures. In the last decades, several zigzag models have been presented (Di Sciuva [7], Cho and Parmerter [8], Icardi [9], Averill [10] and Murakami [11]).

The recent Refined Zigzag Theory (RZT), originally proposed by Tessler et al. [12,13], addressed some drawbacks of the originally developed zigzag model proposed by Di Sciuva [7], such as C^1-continuity and transverse shear stress inconsistencies at clamped boundaries. Starting from the FSDT kinematics, the RZT involves only seven kinematic unknowns and, thanks to the linear zigzag function formulation, it correctly represents the shear deformability of a wide range of laminate configurations without using any shear correction factor. In addition, it requires only C^0-continuity for the selection of shape functions in the finite element approximation. The interest in this efficient and accurate theory is testified by the number of recently published works. The RZT has been applied to the study of multilayered composite and sandwich beam [14–16], plate [17,18] and shell [19] structures. The superior predictivity capabilities of the RZT have been demonstrated even for functionally graded laminated structures [20–22], highly heterogeneous and damaged beams [23–27] and non-linear buckling analysis [28,29]. Recently, RZT has been applied in conjunction with the Iso-Geometric Analysis (IGA) to the analysis of complex laminated structures by Hasim et al. [30–32]. The mixed variational formulation based on the Reissner's Mixed Variational Theorem (RMVT) has been used in conjunction with the RZT to obtain a new mixed-model, i.e. the $RZT^{(m)}$, with the ability to model the parabolic distribution of the transverse shear stresses along the thickness direction, as reported in Refs. [33–37]. Moreover, a variety of different C^0 finite elements has been presented in recent years for the response analysis of beams [14,15,38], plates [17,39–43] and shells [19,40,44].

Although low-order C^0 finite elements are computationally efficient, they commonly suffer from the shear-locking problem [45] when they are used to address the structural response of thin-to-ultra-thin multilayered plates. In such cases, the formulated elements are too stiff since, due to the low-order interpolation strategy, the shear strain energy is too large compared with the bending one [46]. To the author's knowledge, different procedures that address this issue are available in the current literature: the reduced integration [47], the constrained assumed strain field [48], the

Discrete Kirchhoff Theory (DKT) [49,50], the Discrete Shear Gap (DSG) method [51] and the Mixed Interpolation of Tensorial Components (MITC) [52,53]. An alternative approach to overcome the shear-locking issue based on the choice of the shape functions has been proposed by Tessler and Dong [54] for beam elements based on the Timoshenko theory. According to Ref. [54], the transverse displacement requires to be approximated with shape functions whose polynomial order is one-degree higher with respect to those used for the other kinematic variables. The additional node is then condensed out by an appropriate constraining technique to achieve the simplest element topology. The interdependent interpolation, aka *anisoparametric constrained interpolation*, does not require any reduced integration approach and leads to the formulation of variationally consistent elements. This strategy has been successfully applied in RZT framework for beams [14,38] and plates [39,41,43], and to RZT$^{(m)}$ plate formulation [35]. Although this approach addresses the shear-locking for thin structures with a span-to-thickness ratio up to $10^3/10^4$, it has been observed in Refs. [40,41] that the problem holds in ultra-thin regimes, for slenderness values higher than 10^4. Keeping the previous advantages of the *anisoparametric constrained interpolation* and being inspired by Tessler and Hughes works [55,56], in Sorrenti et al. [57] an appropriate Element Shear Correction (ESC) factor has been developed through the Strain Energy Matching (SEM) technique and implemented in a RZT-based quadrilateral element for the analysis of ultra-thin multilayered plates. The promising ZTQ4c element has shown to be faster in convergence behaviour, well-conditioned for a wide range of length-to-thickness ratios and remarkably accurate in predicting strain and stress distributions for cross-ply and sandwich plates.

A further refinement of the RZT kinematics has been proposed, recently, by Sorrenti and Di Sciuva [58], i.e. the enhanced-Refined Zigzag Theory (en-RZT). In the en-RZT, the local in-plane displacement refinement has been enriched by two additional zigzag functions (compared to the original RZT). These functions introduce, at the displacement field level and through the partial interlaminar stress continuity, the transverse shear strain coupling typical of more general lamination schemes, such as angle-ply ones [3]. This coupling effect cannot be addressed by the original RZT due to its formulation; in fact, as observed in Kreja and Sabik's work [59], the zigzag functions vanish, and the standard RZT degenerates into the FSDT when angle-ply lamination schemes are considered. In contrast, the en-RZT, with its enhanced displacement field, is fully capable of providing an accurate representation of the in-plane and through-the-thickness stress distributions for angle-ply stacking sequences, as demonstrated in Ref. [58]. Furthermore, the en-RZT combined with the approximated Ritz method, has been used to estimate the natural

frequencies and buckling loads of different symmetric and anti-symmetric angle-ply plates under different boundary conditions and lamina orientation angles in Refs. [60,61].

This paper aims to formulate a class of robust and efficient three-node triangular (TRIA3) and four-node quadrilateral (QUAD4) finite elements based on the en-RZT for the analysis of general laminates from moderately thick to ultra-thin. In Section 2, the kinematics of the en-RZT for general multilayered plates is presented and the constitutive relations are briefly recalled. In Section 3, using the d'Alembert principle, the en-RZT finite element formulation for triangular and quadrilateral element topologies is presented, together with the adoption of the *anisoparametric constrained* strategy and the ESC factor. In Section 4, some numerical examples are considered to assess the convergence behaviour of the proposed elements for bending and free-vibration problems. The effect of mesh distortion, of the edge length-to-thickness ratio are investigated in order to evaluate the elements' performance from thick to ultra-thin plate regimes. Subsequently, the newly developed elements are compared with high-fidelity three-dimensional FE models for the global (deflection and natural frequencies) and local analysis (in-plane displacements and strains) of angle-ply lamination schemes.

2. Enhanced-Refined Zigzag Theory kinematics, strains, stresses and constitutive relations

This Section briefly recalls the basic assumptions and definitions of the enhanced-Refined Zigzag Theory (en-RZT) for general multilayered plates.

2.1. Displacement field

Let us consider a multilayered flat plate made of N perfectly bonded orthotropic layers. Assuming as V the plate volume, h is the thickness, the points of the plate are referred to an orthogonal Cartesian coordinate system $\mathbf{X}=\{x_i\}\ (i=1,2,3)$, where the vector $\mathbf{x}=\{x_\alpha\}\ (\alpha=1,2)$ represents the set of the in-plane coordinates of the reference surface. According to Figure 1, S is the total cylindrical edge surface, comprised of S_U, the surface portion on which the displacements are prescribed and S_σ, the portion on which the traction forces are prescribed. Moreover, $\bar{p}_B$ and $\bar{p}_T$ are the prescribed pressures acting on the plate's bottom (B) and top (T) surfaces along the transverse coordinate axis x_3. If not otherwise stated, the prescribed quantities are indicated with an overbar.

The reference surface of the plate, referred with the symbol Ω, is chosen to be the middle plane of the plate, and x_3 represents the coordinate direction normal to it, so that $x_3 \in \left[x_{3(B)}, x_{3(T)}\right] \equiv \left[-h/2, +h/2\right]$ and the points belonging to Ω are those with $x_3 = 0$. Moreover,

$\Gamma = S \cap \Omega = \Gamma_U \cup \Gamma_\sigma \left(\Gamma_U \cap \Gamma_\sigma = \varnothing\right)$ is the contour line of Ω, with $\Gamma_U = S_U \cap \Omega$ and $\Gamma_\sigma = S_\sigma \cap \Omega$.

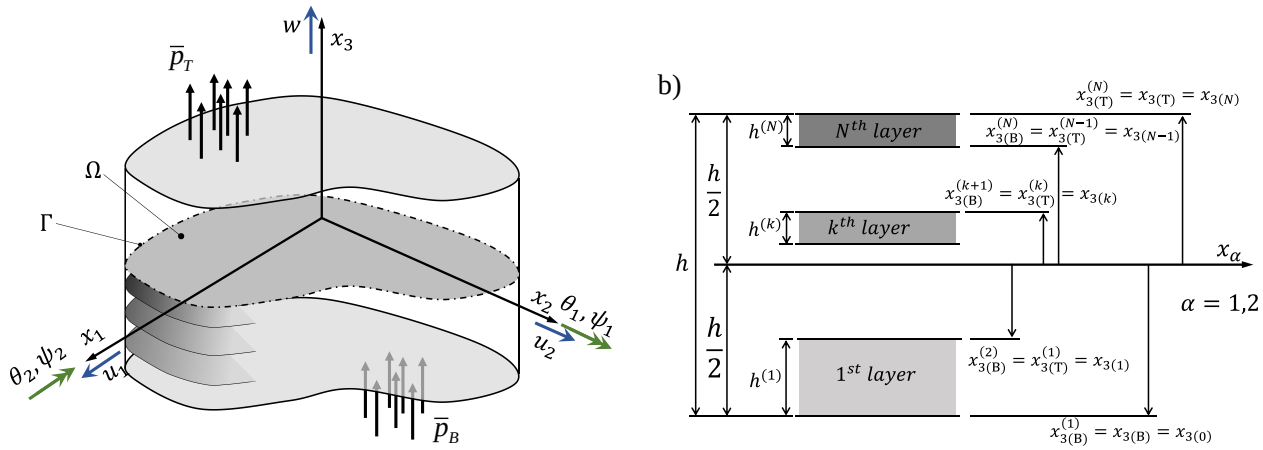

Figure 1: a) General plate notation, loads, en-RZT kinematics variables; b) layer nomenclature.

If not otherwise stated, the superscript $(\bullet)^{(k)}$ is used to indicate quantities corresponding to the k^{th} layer (k=1,…,N), whereas the subscript $(\bullet)_{(k)}$ (k=1,…,N-1) stands for the quantity $(\bullet)$ valued at $x_3 = x_{3(k)}$, i.e. at the k^{th} interface (k=1,…,N-1) between the k^{th} and the $(k+1)^{\text{th}}$ layer. In addition, subscripts (B) and (T) indicate the bottom and top surfaces of a single layer/whole plate, respectively. Specifically, as it is reported in Figure 1b , $x_{3(\text{B})}^{(1)} = x_{3(\text{B})}$ and $x_{3(\text{T})}^{(N)} = x_{3(\text{T})}$ denote the transverse coordinates of the bottom and top surfaces of the whole plate; thus, $h = x_{3(\text{T})} - x_{3(\text{B})}$ is the total plate thickness and $h^{(k)} = x_{3(k)} - x_{3(k-1)} = x_{3(\text{T})}^{(k)} - x_{3(\text{B})}^{(k)}$ $(k = 1,2,...,N)$, the thickness of the k^{th} layer. If not otherwise specified, the Einstein summation convention over repeated indices is adopted, with Latin indices ranging from 1 to 3 and Greek indices ranging from 1 to 2. The thickness of each layer, as well as of the whole plate, is assumed to be constant. Additionally, the symbol $(\bullet)_{,i} = \partial(\bullet)/\partial x_i$ refers to the derivative of the function with the respect to the coordinate axis x_i. An overdot indicates differentiation with respect to the time.

The expression of the plate displacement field, according to the enhanced Refined Zigzag Theory (en-RZT) [58], follows:

$$\begin{aligned} U_1^{(k)}(\mathbf{x}, x_3; t) &= u_1(\mathbf{x}; t) + x_3\theta_1(\mathbf{x}; t) + \phi_{11}^{(k)}(x_3)\psi_1(\mathbf{x}; t) + \phi_{12}^{(k)}(x_3)\psi_2(\mathbf{x}; t) \\ U_2^{(k)}(\mathbf{x}, x_3; t) &= u_2(\mathbf{x}; t) + x_3\theta_2(\mathbf{x}; t) + \phi_{21}^{(k)}(x_3)\psi_1(\mathbf{x}; t) + \phi_{22}^{(k)}(x_3)\psi_2(\mathbf{x}; t) \\ U_3(\mathbf{x}, x_3; t) &= w(\mathbf{x}; t) \end{aligned} \tag{1}$$

where $U_1^{(k)}$, $U_2^{(k)}$ and U_3 are the orthogonal components of the displacement vector along (x_1, x_2, x_3) respectively. The transverse displacement w is assumed to be constant along the thickness direction, thus $\varepsilon_{33} = U_{3,3} = 0$. The quantities $\mathbf{u}^T(\mathbf{x};t) = \lfloor u_1(\mathbf{x};t) \quad u_2(\mathbf{x};t) \rfloor$ are the uniform in-plane displacements, $\boldsymbol{\theta}^T(\mathbf{x};t) = \lfloor \theta_1(\mathbf{x};t) \quad \theta_2(\mathbf{x};t) \rfloor$ the average bending rotations and $\boldsymbol{\psi}^T(\mathbf{x};t) = \lfloor \psi_1(\mathbf{x};t) \quad \psi_2(\mathbf{x};t) \rfloor$ the zigzag rotations.

Moreover,

$$\boldsymbol{\varphi}^{(k)}(x_3) = \begin{bmatrix} \phi_{11}^{(k)}(x_3) & \phi_{12}^{(k)}(x_3) \\ \phi_{21}^{(k)}(x_3) & \phi_{22}^{(k)}(x_3) \end{bmatrix} \tag{2}$$

is the set of through-the-thickness piecewise linear and continuous zigzag functions which depend only on the thickness and transformed transverse shear moduli of each layer, as a results of the partial transverse shear stress continuity across the laminate interfaces. According to the formulation reported in Ref. [58], this set of zigzag function given by Eq. (2) takes into account for angle-ply lamination schemes the coupling effect between the two zigzag rotations. Additionally, these functions are enforced to vanish on the bottom and top external surfaces of the plate, i.e. $\boldsymbol{\varphi}^{(1)}(-h/2) = \boldsymbol{\varphi}^{(N)}(+h/2) = \mathbf{0}$. According to the Refs. [58,60], their expression for the k^{th} layer is here reported:

$$\begin{aligned} \boldsymbol{\varphi}^{(k)}(x_3) &= \left(x_3 - x_{3(\mathrm{B})}\right)\left(\mathbf{S}_{\mathrm{t}}^{(k)}\mathbf{G} - \mathbf{I}\right) + \sum_{r=1}^{k} h^{(r)}\left(\mathbf{S}_{\mathrm{t}}^{(r)} - \mathbf{S}_{\mathrm{t}}^{(k)}\right)\mathbf{G} \\ &= \left(x_3 - x_{3(\mathrm{B})}\right)\boldsymbol{\beta}^{(k)} + \sum_{r=1}^{k} h^{(r)}\left(\boldsymbol{\beta}^{(r)} - \boldsymbol{\beta}^{(k)}\right) \qquad (k = 1,\ldots,N) \end{aligned} \tag{3}$$

where

$$\boldsymbol{\beta}^{(k)} = \mathbf{S}_t^{(k)}\mathbf{G} - \mathbf{I}; \quad \mathbf{G} = h\left(\sum_{k=1}^{N} h^{(k)}\mathbf{S}_t^{(k)}\right)^{-1} \tag{4}$$

and $\mathbf{S}_t^{(k)} = \left(\breve{\mathbf{C}}_t^{(k)}\right)^{-1}$ is the symmetric matrix of the transverse shear compliance coefficients of the k^{th} layer. Note that in Eq. (3), the summation of index *"r"* from 1 to the k^{th} layer considers the effect of the previous layers on the correct evaluation of the through-the-thickness distribution of the zigzag functions across the k^{th} layer.

Assuming the linear strain-displacement relations, the strain components are obtained as follows:

$$\boldsymbol{\varepsilon}_p^{(k)}\left(\mathbf{x},x_3;t\right)=\begin{Bmatrix} U_{1,1}^{(k)}\left(\mathbf{x},x_3;t\right) \\ U_{2,2}^{(k)}\left(\mathbf{x},x_3;t\right) \\ U_{1,2}^{(k)}\left(\mathbf{x},x_3;t\right)+U_{2,1}^{(k)}\left(\mathbf{x},x_3;t\right) \end{Bmatrix}=\begin{Bmatrix} \varepsilon_{11}^{(k)}\left(\mathbf{x},x_3;t\right) \\ \varepsilon_{22}^{(k)}\left(\mathbf{x},x_3;t\right) \\ \gamma_{12}^{(k)}\left(\mathbf{x},x_3;t\right) \end{Bmatrix}$$
$$\boldsymbol{\gamma}_t^{(k)}\left(\mathbf{x},x_3;t\right)=\begin{Bmatrix} U_{1,3}^{(k)}\left(\mathbf{x},x_3;t\right)+U_{3,1}\left(\mathbf{x},x_3;t\right) \\ U_{2,3}^{(k)}\left(\mathbf{x},x_3;t\right)+U_{3,2}\left(\mathbf{x},x_3;t\right) \end{Bmatrix}=\begin{Bmatrix} \gamma_{13}^{(k)}\left(\mathbf{x},x_3;t\right) \\ \gamma_{23}^{(k)}\left(\mathbf{x},x_3;t\right) \end{Bmatrix} \tag{5}$$

Taking into account the en-RZT kinematics, Eq. (5) can be rewritten:

$$\begin{Bmatrix} \boldsymbol{\varepsilon}_{\mathrm{p}}^{(k)}\left(\mathbf{x},x_3;t\right) \\ \boldsymbol{\gamma}_t^{(k)}\left(\mathbf{x},x_3;t\right) \end{Bmatrix}=\begin{bmatrix} \mathbf{I} & x_3\mathbf{I} & \boldsymbol{\Phi}^{(k)}(x_3) & \mathbf{0} & \mathbf{0} \\ \mathbf{0} & \mathbf{0} & \mathbf{0} & \mathbf{I} & \boldsymbol{\beta}^{(k)}(x_3) \end{bmatrix}\begin{Bmatrix} \boldsymbol{\varepsilon}_m\left(\mathbf{x};t\right) \\ \boldsymbol{\varepsilon}_\theta\left(\mathbf{x};t\right) \\ \boldsymbol{\varepsilon}_\psi\left(\mathbf{x};t\right) \\ \boldsymbol{\gamma}^{(0)}\left(\mathbf{x};t\right) \\ \boldsymbol{\psi}\left(\mathbf{x};t\right) \end{Bmatrix}=\mathbf{Z}_\varepsilon(x_3)\begin{Bmatrix} \boldsymbol{\varepsilon}_m\left(\mathbf{x};t\right) \\ \boldsymbol{\varepsilon}_\theta\left(\mathbf{x};t\right) \\ \boldsymbol{\varepsilon}_\psi\left(\mathbf{x};t\right) \\ \boldsymbol{\gamma}^{(0)}\left(\mathbf{x};t\right) \\ \boldsymbol{\psi}\left(\mathbf{x};t\right) \end{Bmatrix} \tag{6}$$

where

$$\begin{aligned} \boldsymbol{\varepsilon}_m^T\left(\mathbf{x};t\right)&=\begin{bmatrix} u_{1,1}\left(\mathbf{x};t\right) & u_{2,2}\left(\mathbf{x};t\right) & u_{1,2}\left(\mathbf{x};t\right)+u_{2,1}\left(\mathbf{x};t\right) \end{bmatrix} \\ \boldsymbol{\varepsilon}_\theta^T\left(\mathbf{x};t\right)&=\begin{bmatrix} \theta_{1,1}\left(\mathbf{x};t\right) & \theta_{2,2}\left(\mathbf{x};t\right) & \theta_{1,2}\left(\mathbf{x};t\right)+\theta_{2,1}\left(\mathbf{x};t\right) \end{bmatrix} \end{aligned} \tag{7}$$

$$\boldsymbol{\varepsilon}_\psi^T\left(\mathbf{x};t\right)=\begin{bmatrix} \psi_{1,1}\left(\mathbf{x};t\right) & \psi_{2,2}\left(\mathbf{x};t\right) & \psi_{1,2}\left(\mathbf{x};t\right) & \psi_{2,1}\left(\mathbf{x};t\right) \end{bmatrix}$$

$$\boldsymbol{\Phi}^{(k)}(x_3)=\begin{bmatrix} \phi_{11}^{(k)}(x_3) & 0 & 0 & \phi_{12}^{(k)}(x_3) \\ 0 & \phi_{22}^{(k)}(x_3) & \phi_{21}^{(k)}(x_3) & 0 \\ \phi_{21}^{(k)}(x_3) & \phi_{12}^{(k)}(x_3) & \phi_{11}^{(k)}(x_3) & \phi_{22}^{(k)}(x_3) \end{bmatrix} \tag{8}$$

$$\boldsymbol{\gamma}^{(0)}\left(\mathbf{x};t\right)=\begin{Bmatrix} \gamma_1^{(0)}\left(\mathbf{x};t\right) \\ \gamma_2^{(0)}\left(\mathbf{x};t\right) \end{Bmatrix}=\begin{Bmatrix} \theta_1\left(\mathbf{x};t\right)+w_{,1}\left(\mathbf{x};t\right) \\ \theta_2\left(\mathbf{x};t\right)+w_{,2}\left(\mathbf{x};t\right) \end{Bmatrix}=\boldsymbol{\theta}\left(\mathbf{x};t\right)+\partial\mathbf{w}\left(\mathbf{x};t\right) \tag{9}$$

and

$$\partial\mathbf{w}^T\left(\mathbf{x};t\right)=\begin{bmatrix} w_{,1}\left(\mathbf{x};t\right) & w_{,2}\left(\mathbf{x};t\right) \end{bmatrix};\quad \boldsymbol{\beta}^{(k)}(x_3)=\frac{\partial\boldsymbol{\varphi}^{(k)}(x_3)}{\partial x_3} \tag{10}$$

The material of each layer is assumed to be linear elastic and orthotropic, with a plane of symmetry parallel to the reference surface. However, its principal orthotropy directions (material axes) are arbitrarily oriented with an angle $\mathrm{Y}^{(k)}$ with respect to the x_1 axis. Note that in Eq. (6), for general lamination schemes, $\boldsymbol{\beta}^{(k)}$ is a full matrix; thus, the transverse shear strain components, i.e. $\gamma_{13}^{(k)}$ and $\gamma_{23}^{(k)}$, are influenced by both zigzag rotations. As demonstrated in Ref. [58], this effect contributes in a more accurate structural prediction of the displacements, strains and stresses in such laminates.

By neglecting the transverse normal stress, i.e. $\sigma_{33}=0$, as usual in thin and moderately thick structures, the linear elastic constitutive relations can be written as follows:

$$\begin{Bmatrix} \boldsymbol{\sigma}_p^{(k)}\left(\mathbf{x},x_3;t\right) \\ \boldsymbol{\tau}_t^{(k)}\left(\mathbf{x},x_3;t\right) \end{Bmatrix} = \begin{bmatrix} \breve{\mathbf{C}}_p^{(k)} & \mathbf{0} \\ \mathbf{0} & \breve{\mathbf{C}}_t^{(k)} \end{bmatrix} \begin{Bmatrix} \boldsymbol{\varepsilon}_p^{(k)}\left(\mathbf{x},x_3;t\right) \\ \boldsymbol{\gamma}_t^{(k)}\left(\mathbf{x},x_3;t\right) \end{Bmatrix} \tag{11}$$

where $\boldsymbol{\sigma}_p^{(k)T}\left(\mathbf{x},x_3;t\right) = \begin{bmatrix} \sigma_{11}^{(k)} & \sigma_{22}^{(k)} & \tau_{12}^{(k)} \end{bmatrix}$ and $\boldsymbol{\tau}_t^{(k)T}\left(\mathbf{x},x_3;t\right) = \begin{bmatrix} \tau_{13}^{(k)} & \tau_{23}^{(k)} \end{bmatrix}$ are the in-plane and transverse shear stress components, respectively. Moreover, $\breve{\mathbf{C}}_p^{(k)} = \left[\breve{C}_{ij}\right](i,j=1,2,6)$ and $\breve{\mathbf{C}}_t^{(k)} = \left[\breve{C}_{\alpha\beta}\right](\alpha,\beta=4,5)$ are, respectively, the in-plane reduced and transverse shear elastic stiffness coefficients of the k^{th} layer expressed in the plate axes.

2.2. Governing equations via the Principle of Virtual Displacements

The governing equations and the variationally consistent boundary conditions are derived using the dynamic version of the Principle of Virtual Displacements (PVDs), also known as d'Alembert principle.

Assuming the symbol δ for the variational operator, the principle expresses as follow:

$$\delta W_{\text{int}} - \delta W_{\text{ext}} = \delta W_{\text{in}} \tag{12}$$

where

$$\delta W_{\text{int}} = \int_V \left(\delta\boldsymbol{\varepsilon}_p^{(k)T}\boldsymbol{\sigma}_p^{(k)} + \delta\boldsymbol{\gamma}_t^{(k)T}\boldsymbol{\tau}_t^{(k)}\right)dV \tag{13}$$

is the virtual variation of the internal work given by the stresses;

$$\delta W_{\text{in}} = -\int_\Omega \left\langle \rho^{(k)}(x_3)\delta\mathbf{U}^T\ddot{\mathbf{U}} \right\rangle d\Omega \tag{14}$$

is the virtual work of inertia forces. In Eq. (14), $\rho^{(k)}(x_3)$ is the material mass density and $\mathbf{U}^T\left(\mathbf{X};t\right) = \begin{bmatrix} U_1^{(k)} & U_2^{(k)} & U_3 \end{bmatrix}$ is the vector of the displacement components.

Furthermore, δW_{ext} is the virtual work of external loads:

$$\delta W_{\text{ext}} = \int_\Omega \boldsymbol{\delta} w \bar{p}_3 d\Omega \tag{15}$$

where $\bar{p}_3 = \bar{p}_B\left(\mathbf{x};t\right) + \bar{p}_T\left(\mathbf{x};t\right)$, and no shear tractions are acting on top and bottom surfaces. In addition, the integration along the thickness direction shown in the previous formulas can be performed according to the following expression $\left\langle \bullet \right\rangle = \sum_{k=1}^{N} \int_{x_3^{(k-1)}}^{x_3^{(k)}} (\bullet) dx_3 = \sum_{k=1}^{N} \int_{x_{3(\mathrm{B})}^{(k)}}^{x_{3(\mathrm{T})}^{(k)}} (\bullet) dx_3$.

Substituting the expression of the stress relations, i.e. Eq. (11) , into the expression of the virtual variation of internal energy, Eq. (13) and integrating along the thickness direction, yields:

$$\delta W_{\text{int}} = \int_\Omega \left(\delta\boldsymbol{\varepsilon}_m{}^T\mathbf{N} + \delta\boldsymbol{\varepsilon}_\theta{}^T\mathbf{M} + \delta\boldsymbol{\varepsilon}_\psi{}^T\mathbf{M}^\phi + \delta\boldsymbol{\gamma}^{(0)T}\mathbf{Q} + \delta\boldsymbol{\psi}^T\mathbf{Q}^\phi\right)d\Omega \tag{16}$$

In Eq. (16), the following force and moment stress resultants for unit length have been introduced:

$$\left(\mathbf{N},\mathbf{M},\mathbf{M}^{\phi}\right)=\left(\left\{\begin{matrix}N_{11}\\N_{22}\\N_{12}\end{matrix}\right\},\left\{\begin{matrix}M_{11}\\M_{22}\\M_{12}\end{matrix}\right\},\left\{\begin{matrix}M_{11}^{\phi}\\M_{22}^{\phi}\\M_{12}^{\phi}\\M_{21}^{\phi}\end{matrix}\right\}\right)=\left\langle\left(1,x_3,\boldsymbol{\varphi}^{(k)T}\right)\boldsymbol{\sigma}_{\mathrm{p}}^{(k)}\right\rangle \tag{17}$$

$$\left(\mathbf{Q},\mathbf{Q}^{\phi}\right)=\left(\left\{\begin{matrix}Q_1\\Q_2\end{matrix}\right\},\left\{\begin{matrix}Q_1^{\phi}\\Q_2^{\phi}\end{matrix}\right\}\right)=\left\langle\left(1,\boldsymbol{\beta}^{(k)}\right)\boldsymbol{\tau}_t^{(k)}\right\rangle \tag{18}$$

Taking into account Eqs. (11) and (6) into Eqs. (17) and (18), yields the en-RZT plate constitutive relation

$$\left\{\begin{matrix}\mathbf{N}\\\mathbf{M}\\\mathbf{M}^{\phi}\\\mathbf{Q}\\\mathbf{Q}^{\phi}\end{matrix}\right\}=\left[\begin{matrix}\mathbf{A}&\mathbf{B}&\mathbf{A}^{\phi}&\mathbf{0}&\mathbf{0}\\\mathbf{B}^{T}&\mathbf{D}&\mathbf{B}^{\phi}&\mathbf{0}&\mathbf{0}\\\mathbf{A}^{\phi T}&\mathbf{B}^{\phi T}&\mathbf{D}^{\phi}&\mathbf{0}&\mathbf{0}\\\mathbf{0}&\mathbf{0}&\mathbf{0}&\mathbf{A}_t&\mathbf{B}_t\\\mathbf{0}&\mathbf{0}&\mathbf{0}&\mathbf{B}_t^{T}&\mathbf{D}_t\end{matrix}\right]\left\{\begin{matrix}\boldsymbol{\varepsilon}_m\\\boldsymbol{\varepsilon}_\theta\\\boldsymbol{\varepsilon}_\psi\\\boldsymbol{\gamma}^{(0)}\\\boldsymbol{\psi}\end{matrix}\right\}=\hat{\mathbf{D}}\left\{\begin{matrix}\boldsymbol{\varepsilon}_m\\\boldsymbol{\varepsilon}_\theta\\\boldsymbol{\varepsilon}_\psi\\\boldsymbol{\gamma}^{(0)}\\\boldsymbol{\psi}\end{matrix}\right\} \tag{19}$$

where

$$\begin{aligned}&\left(\mathbf{A},\mathbf{B},\mathbf{D}\right)=\left\langle\left(1,x_3,x_3^2\right)\breve{\mathbf{C}}_p^{(k)}\right\rangle,\ \left(\mathbf{A}^{\phi},\mathbf{B}^{\phi},\mathbf{D}^{\phi}\right)=\left\langle\left(1,x_3,\boldsymbol{\Phi}^{(k)T}\right)\breve{\mathbf{C}}_p^{(k)}\boldsymbol{\Phi}^{(k)}\right\rangle\\&\left(\mathbf{A}_t,\mathbf{B}_t\right)=\left\langle\left(1,\boldsymbol{\beta}^{(k)}\right)\breve{\mathbf{C}}_t^{(k)}\right\rangle,\ \mathbf{D}_t=\left\langle\boldsymbol{\beta}^{(k)T}\breve{\mathbf{C}}_t^{(k)}\boldsymbol{\beta}^{(k)}\right\rangle\end{aligned} \tag{20}$$

Substituting the full expression of the displacement components according to the en-RZT kinematics, Eq. (1) into Eq. (14) and performing the integration along the thickness direction, the virtual work of inertia forces is rewritten as follows:

$$\delta W_{\mathrm{in}}=-\int_{\Omega}\delta\mathbf{d}^{T}\left[\begin{matrix}\mathbf{m}^{(0)}&0&\mathbf{m}^{(1)}&\mathbf{m}_{\phi}^{(0)}\\0&m^{(0)}&\mathbf{0}&\mathbf{0}\\\mathbf{m}^{(1)}&\mathbf{0}^{T}&\mathbf{m}^{(2)}&\mathbf{m}_{\phi}^{(1)}\\\mathbf{m}_{\phi}^{(0)T}&\mathbf{0}^{T}&\mathbf{m}_{\phi}^{(1)T}&\mathbf{m}_{\phi}^{(2)}\end{matrix}\right]\ddot{\mathbf{d}}\,d\Omega=-\int_{\Omega}\delta\mathbf{d}^{T}\mathbf{m}\ddot{\mathbf{d}}\,d\Omega \tag{21}$$

where, $\mathbf{d}^{T}=\lfloor u_1\quad u_2\quad w\quad\theta_1\quad\theta_2\quad\psi_1\quad\psi_2\rfloor$ and the inertia resultant quantities are defined as follows:

$$\begin{aligned}&m^{(0)}=\left\langle\rho^{(k)}\right\rangle;\quad\left(\mathbf{m}^{(0)},\mathbf{m}^{(1)},\mathbf{m}^{(0)}\right)=\left\langle\rho^{(k)}(1,x_3,x_3^2)\right\rangle\mathbf{I};\\&\left(\mathbf{m}_{\phi}^{(0)},\mathbf{m}_{\phi}^{(1)},\mathbf{m}_{\phi}^{(2)}\right)=\left\langle\rho^{(k)}(\mathbf{I},x_3\mathbf{I},\boldsymbol{\varphi}^{(k)T})\boldsymbol{\varphi}^{(k)}\right\rangle\end{aligned} \tag{22}$$

Finally, integrating by parts the governing functional, Eq. (12), and its contributions, Eqs. (13)-(21), the governing equations in terms of the kinematic variables are obtained. For static problems, the full expression of equilibrium equations is reported in [58].

3. Finite element formulation

In this Section, triangular and quadrilateral plate elements are formulated according to the en-RZT kinematics.

According to Eq. (16), only the first derivatives of the kinematic variables appear in the d'Alembert's variational statement. Thus, only C^0-continous shape functions are required to formulate consistent finite elements. Clearly, as observed in Ref. [41], such elements suffer of the shear locking problem. In order to circumvent this issue and to obtain efficient and robust triangular and quadrilateral finite elements, two successful strategies are implemented in element formulation: the *anisoparametric constrained interpolation* scheme and the adoption of an Element Shear Correction (ESC) factor.

3.1. Anisoparametric constrained interpolation scheme

In the anisoparametric interpolation scheme, the transverse displacement variable is interpolated using polynomials with one degree higher than those used for in-plane uniform displacements, bending and zigzag rotations. Assuming that the transverse displacement requires quadratic shape functions, the linear-Lagrangian ones are sufficient for the other kinematic variables. Indicating with N_{nw} the number of nodes necessary to interpolate the transverse displacement and with N_n the number of nodes required for the interpolation of the other kinematic variables, the anisoparametric interpolation scheme expressions read:

$$\begin{aligned} u_\alpha(\mathbf{x};t) &= \sum_{i=1}^{N_n} L_i(\mathbf{x}) u_\alpha^{(i)}(t) \quad \alpha = 1,2 \qquad w(\mathbf{x};t) = \sum_{i=1}^{N_{nw}} P_i(\mathbf{x}) w^{(i)} \\ \theta_\alpha(\mathbf{x};t) &= \sum_{i=1}^{N_n} L_i(\mathbf{x}) \theta_\alpha^{(i)}(t) \quad \alpha = 1,2 \qquad \psi_\alpha(\mathbf{x};t) = \sum_{i=1}^{N_n} L_i(\mathbf{x}) \psi_\alpha^{(i)}(t) \quad \alpha = 1,2 \end{aligned} \tag{23}$$

where in Eq. (23), $N_n = 3$ and $N_{nw} = 6$ for triangular en-RZT elements, and $N_n = 4$ and $N_{nw} = 8$ for quadrilateral ones. In addition to the aforementioned linear Lagrangian shape functions, i.e. $L_i(\mathbf{x})$, $P_i(\mathbf{x})$ are the quadratic shape functions for triangular elements and the serendipity quadratic shape functions for quadrilateral ones. For the sake of clarity, their expression are reported in Appendix A.

This approach is able to reduce the occurrence of shear-locking in various element configurations. In addition, the earlier element topology can be further simplified to achieve a simple TRIA3 and QUAD4 element configuration, by condensing out the mid-edge nodes. The RZT edge-constraint strategy firstly developed by Versino et al. [39,40], defines a local orthogonal edge coordinate system, according to Figure 2, where the *s* is the coordinate along the element's edge and *n* is the orthogonal normal direction. Thus, at the element level the following constraint condition is enforced (see Refs. [39,40] for further details):

$$\eta_{s3,s} = \gamma_{s3,s} - \psi_{n,s} = 0 \tag{24}$$

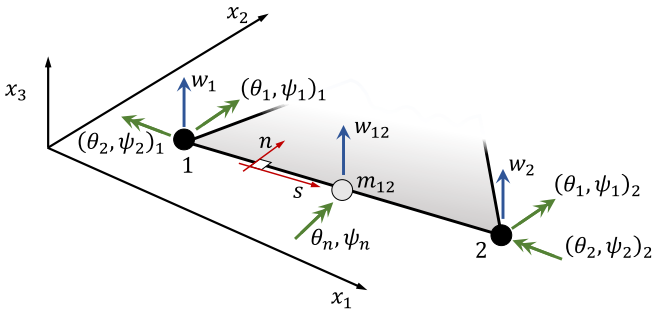

Figure 2: Example for edge quantities in constraint conditions.

Consequently, a new approximation for the transverse displacement is recalled by performing this constraint for each element edge:

$$w = \sum_i^{N_n} L_i w^{(i)} + \sum_i^{N_n} S_{\theta_1}^{(i)} \theta_1^{(i)} + \sum_i^{N_n} S_{\theta_2}^{(i)} \theta_2^{(i)} + \sum_i^{N_n} S_{\psi_1}^{(i)} \psi_1^{(i)} + \sum_i^{N_n} S_{\psi_2}^{(i)} \psi_2^{(i)} \tag{25}$$

where $S_{\theta_1}^{(i)}$, $S_{\theta_2}^{(i)}$, $S_{\psi_1}^{(i)}$ and $S_{\psi_2}^{(i)}$ are the new quadratic shape functions (their full expression is reported for the sake of brevity in Appendix A). Table 1 presents the initial (unconstrained) and final (constrained) topologies of the newly developed en-RZT elements. Hereafter, the following acronyms denote the new formulated elements: the en-RZT-based Triangular 3-node constrained element (enRZT-T3c) and the en-RZT-based Quadrilateral 4-node constrained element (enRZT-Q4c).

Table 1: Triangular (TRIA) and quadrilateral (QUAD) element topologies and nomenclatures.

Initial topology of TRIA and QUAD finite element based	Constraint conditions along element edges	Final topology of TRIA and QUAD constrained elements
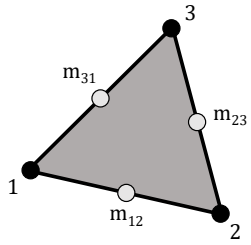	$\eta_{s3,s} = \gamma_{s3,s} - \psi_{n,s} = 0$ 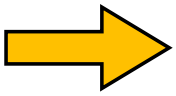	**enRZT-T3c** 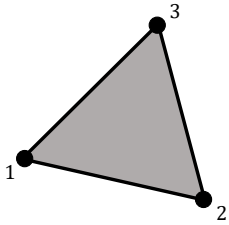
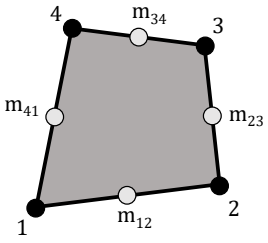		**enRZT-Q4c** 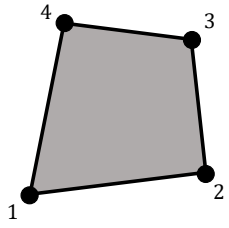
Element's computational cost: 24 dofs (TRIA) 32 dofs (QUAD)	Nodal dofs' symbology: ● $u_1, u_2, w, \theta_1, \theta_2, \psi_1, \psi_2$ ○ w	Element's computational cost: 21 dofs (TRIA) 28 dofs (QUAD)

Introducing the vector of the element kinematic unknowns, i.e. $\mathbf{d}^{(e)T} = \lfloor u_1 \quad u_2 \quad w \quad \theta_1 \quad \theta_2 \quad \psi_1 \quad \psi_2 \rfloor^{(e)}$, and combining Eq. (23) with the new expression for the transverse displacement component, Eq. (25), yields to the following useful expression in matrix notation:

$$\mathbf{d}^{(e)} = \sum_{i=1}^{N_n} \mathbf{N}_i^{(e)} \mathbf{q}_i^{(e)} = \begin{bmatrix} L_i & 0 & 0 & 0 & 0 & 0 & 0 \\ 0 & L_i & 0 & 0 & 0 & 0 & 0 \\ 0 & 0 & L_i & S_{\theta_1}^{(i)} & S_{\theta_2}^{(i)} & S_{\psi_1}^{(i)} & S_{\psi_2}^{(i)} \\ 0 & 0 & 0 & L_i & 0 & 0 & 0 \\ 0 & 0 & 0 & 0 & L_i & 0 & 0 \\ 0 & 0 & 0 & 0 & 0 & L_i & 0 \\ 0 & 0 & 0 & 0 & 0 & 0 & L_i \end{bmatrix}^{(e)} \begin{Bmatrix} u_1^{(i)} \\ u_2^{(i)} \\ w^{(i)} \\ \theta_1^{(i)} \\ \theta_2^{(i)} \\ \psi_1^{(i)} \\ \psi_2^{(i)} \end{Bmatrix}^{(e)} \tag{26}$$

Substituting Eq. (26) into the expression of the strain according to the en-RZT kinematics, i.e. Eq. (6), yields

$$\begin{Bmatrix} \boldsymbol{\varepsilon}_{\mathrm{p}}^{(k)} \\ \boldsymbol{\gamma}_t^{(k)} \end{Bmatrix}^{(e)} = \mathbf{Z}_{\varepsilon} \sum_{i=1}^{N_n} \mathbb{B}_i^{(e)} \mathbf{q}_i^{(e)} \tag{27}$$

where $\mathbb{B}_i^{(e)}$ is the matrix that contains the derivatives of the shape functions. Accordingly, with the definitions given by Eq. (6), the $\mathbb{B}_i^{(e)}$ can be expressed as follows:

$$\mathbb{B}_i^{(e)T} = \lfloor \mathbb{B}_m{}^T \quad \mathbb{B}_\theta{}^T \quad \mathbb{B}_\psi{}^T \quad \mathbb{B}_s{}^T \rfloor_i^{(e)} \tag{28}$$

For the sake of conciseness, the complete expression of each matrix in Eq. (28) is given in Appendix B.

Then, the elemental equations of motion are obtained by substituting Eq. (26) and Eq. (27) into the contributions of the d'Alembert principle, i.e. Eqs. (15), (16) and (21)

$$\mathbf{M}^{(e)} \ddot{\mathbf{q}}^{(e)} + \mathbf{K}^{(e)} \mathbf{q}^{(e)} = \mathbf{P}^{(e)} \tag{29}$$

where the elemental stiffness and mass matrices are expressed as follows

$$\mathbf{K}^{(e)} = \int_{\Omega^{(e)}} \mathbb{B}^{(e)T} \hat{\mathbf{D}} \mathbb{B}^{(e)} d\Omega; \qquad \mathbf{M}^{(e)} = \int_{\Omega^{(e)}} \mathbf{N}^{(e)T} \mathbf{m} \mathbf{N}^{(e)} d\Omega \tag{30}$$

and, finally, the nodal force vector is

$$\mathbf{P}^{(e)T} = \int_{\Omega^{(e)}} \bar{p}_3 \lfloor \mathbf{0} \quad \mathbf{0} \quad \mathbf{L}^{(e)} \quad \mathbf{S}_{\theta 1}^{(e)} \quad \mathbf{S}_{\theta 2}^{(e)} \quad \mathbf{S}_{\psi 1}^{(e)} \quad \mathbf{S}_{\psi 2}^{(e)} \rfloor^T d\Omega + \sum_f^{N_f} \bar{\mathbf{F}}_f(\mathbf{x}_f) \tag{31}$$

with $\bar{\mathbf{F}}_f{}^T = \lfloor 0 \quad 0 \quad \bar{F}_{3f} \quad 0 \quad 0 \quad 0 \quad 0 \rfloor$ the *f-th* nodal force-moment vector applied in the plate $\mathbf{x}_f$ point.

3.2. Appropriate Element Shear Correction (ESC) factor

The sole adoption of the shape functions based on the anisoparametric constrained strategy is insufficient to solve the shear-locking problem definitively, as observed in Refs. [40,41]. By keeping the same mesh size, it has been shown that even the RZT-based elements that include in their formulation the anisoparametric constrained interpolation lock when they reach the ultra-thin regimes (values of slenderness higher than 10^4). A viable solution is the implementation of an appropriate Element Shear Correction (ESC) factor that addresses the element energy balancing between the bending and transverse shear contributions without changing the interpolation scheme adopted for the kinematic variables and strains. Hereafter denoted with $\phi^2_{(e)}$, the ESC factor is implemented in the formulated constrained triangular and quadrilateral en-RZT-based elements, i.e. enRZT-T3c and enRZT-Q4c. Its expression follows:

$$\phi^2_{(e)} = \frac{1}{1+\alpha_{(e)}/C} \tag{32}$$

where C is a constant yet established for RZT on the basis of numerical performances (for further details on the complete formulation, see Ref. [57]). Moreover, $\alpha_{(e)}$ is defined as the trace quantity (*TR*) of the elemental bending ($\mathbf{K}_b^{(e)}$) and transverse shear stiffness ($\mathbf{K}_s^{(e)}$) matrices associated with the bending and zigzag rotations degrees of freedom. Its expression, valid for both triangular and quadrilateral elements, is here recalled for clarity:

$$\alpha_{(e)} \stackrel{def}{=} \frac{TR\left(\mathbf{K}_s^{(e)}(\theta_1,\theta_2,\psi_1,\psi_2)\right)}{TR\left(\mathbf{K}_b^{(e)}(\theta_1,\theta_2,\psi_1,\psi_2)\right)} \tag{33}$$

where the complete expression for $\mathbf{K}_b^{(e)}$ and $\mathbf{K}_s^{(e)}$ valid for en-RZT kinematics is reported in Appendix B. The ESC factor obtained by Eq. (32) is then used in the constitutive en-RZT relations, i.e. Eq. (19) to correct the shear stiffness in the enRZT-T3c/enRZT-Q4c elemental stiffness matrix.

4. Numerical Results

In this Section, the numerical performances of the newly formulated enRZT-T3c and enRZT-Q4c elements are evaluated by addressing bending and free-vibration problems of general multilayered plates. For sake of simplicity, the investigated numerical examples are related to rectangular flat plates with their edges parallel to the axes (x_1, x_2), where the length of the plate along x_1 axis is denoted with a and the width, along x_2 axis, with b. Its origin coincides with the bottom-left corner of the rectangular plate.

In the following numerical analysis, $C=50$ is adopted in Eq. (32), since in Ref. [57] this was found to represent a good compromise to improve ZTQ4c elements convergence behaviour.

Moreover, Table 2 and Table 3 report the nomenclature and mechanical properties of each lamina and the laminate stacking sequences of the plates considered in this numerical assessment.

Table 2: Material nomenclature and properties. The elastic moduli are given in GPa, and the mass density in kg/m^3.

Material name	E_1	E_2	E_3	ν_{12}	ν_{13}	ν_{23}	G_{12}	G_{13}	G_{23}	ρ
A	175	7	7	0.25	0.25	0.25	3.5	3.5	1.4	1
B	15	1	1	0.3	0.3	0.35	0.5	0.5	0.35	1
C	140	10	10	0.3	0.3	0.49	5.330	5.330	3.230	1

Table 3: Laminate stacking sequences (starting from the bottom layer) and nomenclatures. The orientations are given in degrees.

Laminate ID	Normalised thickness $h^{(k)}/h$	Lamina materials	Lamina orientations [°]
L0	[0.3333/0.3333/0.3333]	[A/A/A]	[0/90/0]
L1	[0.5/0.5]	[A/A]	[-15/+15]
L2	$[0.1/0.1]_5$	$[B/B]_5$	$[-45/+45]_5$
L3	[0.25/0.25/0.25/0.25]	[C/C/C/C]	[45/-45/45/-45]
L4	[0.25/0.5/0.25]	(A/A/A)	[30/-30/30]

If not otherwise specified, the following normalised quantities are considered:

$$\bar{w} = 100\frac{h^3 E_2^{(1)}}{\bar{q}_0 a^4} w; \quad \left(\bar{U}_1^{(k)}, \bar{U}_2^{(k)}\right) = 10^3 \frac{h^3 E_2^{(1)}}{\bar{q}_0 a^4}\left(U_1^{(k)}, U_2^{(k)}\right); \quad \bar{f} = f\frac{a^2}{h}\sqrt{\frac{\rho^{(1)}}{E_2^{(1)}}} \tag{34}$$

Note that the quantities expressed in Eq. (34) are also dimensionless.

In the numerical analysis, different sets of boundary conditions are considered to assess how the elements behave. Table 4 summarises which dofs are restrained along the corresponding edge for each case. With reference to the simply-supported case, cross-ply and anti-symmetric angle-ply laminates require specific constraints.

Table 4: List of Boundary Conditions (BCs) considered in this study.

Boundary condition ID	Edge's nodal dofs restrained
Simply Supported (SS-1)	$@\, x_1 = 0, a : u_2 = w = \theta_2 = \psi_2 = 0$ $@\, x_2 = 0, b : u_1 = w = \theta_1 = \psi_1 = 0$
Simply Supported (SS-2)	$@\, x_1 = 0, a : u_1 = w = \theta_2 = \psi_2 = 0$ $@\, x_2 = 0, b : u_2 = w = \theta_1 = \psi_1 = 0$
Clamped (C)	$u_1 = u_2 = w = \theta_1 = \theta_2 = \psi_1 = \psi_2 = 0$
Free (F)	No constraints

For the sake of clarity, the regular mesh patterns considered in this study are reported in Figure 3. Moreover, hereafter the symbology "NEx_1 x NEx_2" indicates the discretization adopted for the investigated plate, where the first number represents the elements along the plate edges in x_1 direction and the second one the elements in x_2 direction.

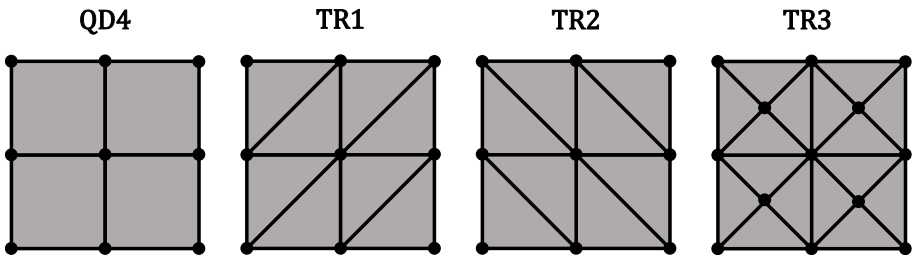

Figure 3: Regular mesh schemes and notation.

When no exact elasticity solution exists, a high-fidelity FE model, obtained by using NASTRAN® solid (HEXA20) elements with quadratic shape functions, is used as a reference solution for comparison. Since the en-RZT performances have been finely addressed in Ref. [62] no particular emphasis is paid on the analytical results.

4.1. Convergence analysis

In this Section, the convergence behaviour of the newly formulated elements is evaluated. This study considers squared (*a/b=1*) cross-ply and anti-symmetric angle-ply multilayered plates simply-supported on all their edges. For the static analysis, a bi-sinusoidal transverse load pressure is applied. The span-to-thickness ratio considered varies from moderately thick to ultra-thin regimes, i.e. a/h=10, 10^3 and 10^6. Due to the lamination schemes, for laminate L0, SS-1 conditions are applied, whereas for laminates L1 and L2, SS-2 boundary conditions are required.

The reference en-RZT analytical solution (whose results in terms of maximum transverse deflection and fundamental frequencies are reported in Table 5) is the exact trigonometric, Navier-type solution of the governing equations for the case of simply supported boundary conditions (refers to [58] for more details).

Table 5: Reference en-RZT analytical results for normalised maximum transverse deflection and fundamental frequency (given values are dimensionless according to Eq. (34)).

	STATIC $\bar{w}$		**MODAL** $\bar{f}$	
a/h	L0	L1	L0	L2
10	0.7402	0.7821	1.8407	2.2085
10^3	0.4313	0.6205	2.4235	2.5431
10^6	0.4312	0.6205	2.4236	2.5431

The mesh-size parameter $\left(p_{ms}\right)$ is introduced as a length characteristic of the mesh discretisation. It represents the minimum length of the element's edges in a regular mesh pattern. The accuracy of the FE results is established by evaluating the estimated error (*ERR*) defined as follows:

$$ERR = \left|(\bullet)_{AN} - (\bullet)_{FEM}\right| \tag{35}$$

where the symbol $(\bullet)_{FEM}$ represents the FE results and $(\bullet)_{AN}$ the analytical ones. More specifically, *ERR* is evaluated for the vector of kinematic variables, i.e. $\mathbf{d}^T = \lfloor u_1 \quad u_2 \quad w \quad \theta_1 \quad \theta_2 \quad \psi_1 \quad \psi_2 \rfloor$, in the case of static analyses and for the fundamental frequency corresponding to the first transverse modal shape in the case of modal analyses.

In addition, it is convenient to introduce for a generic vector $\mathbf{v}$, defined in the space (x_1, x_2), the Sobolev norms of order 0 and order 1 (see Ref. [46]), respectively denoted with the subscripts L^2 and H^1. They reads:

$$\begin{aligned} \|\mathbf{v}\|_{L^2} &= \sqrt{\int_\Omega |\mathbf{v}|^2 \, d\Omega} \\ \|\mathbf{v}\|_{H^1} &= \sqrt{\|\mathbf{v}\|_{L^2}^2 + \|\nabla \mathbf{v}\|_{L^2}^2} \end{aligned} \tag{36}$$

with $\nabla^T(\bullet) = \left\lfloor \partial(\bullet)/\partial x_1 \quad \partial(\bullet)/\partial x_2 \right\rfloor$.

In the following static analyses, the errors related to the kinematic variables, evaluated with Eq. (35), are expressed in terms of L^2 and H^1 norms, to assess the elements' convergence rates. Subsequently, for comparison purposes, the normed errors are normalised with the corresponding norm of the vector of analytical kinematic variables. The estimated normalised normed errors thus read

$$\|ERR_n\|_{L^2} = \frac{\sqrt{\int_\Omega |\mathbf{d}_{AN} - \mathbf{d}_{FEM}|^2 \, d\Omega}}{\sqrt{\int_\Omega |\mathbf{d}_{AN}|^2 \, d\Omega}} \tag{37}$$

$$\|ERR_n\|_{H^1} = \frac{\sqrt{\|\mathbf{d}_{AN} - \mathbf{d}_{FEM}\|_{L^2}^2 + \|\nabla(\mathbf{d}_{AN} - \mathbf{d}_{FEM})\|_{L^2}^2}}{\sqrt{\|\mathbf{d}_{AN}\|_{L^2}^2 + \|\nabla(\mathbf{d}_{AN})\|_{L^2}^2}} \tag{38}$$

The estimated normalised normed errors computed according to the L^2 and H^1 norms (see, Eqs. (37) and (38)) for static bending analysis of simply-supported cross-ply (L0) and antisymmetric angle-ply (L1) laminates under bi-sinusoidal pressure are reported in log-log plots, respectively, in Figure 4 and Figure 5. Moreover, for comparison purposes with the element performances, Figure 4 and Figure 5 report the linear and quadratic convergence rates. These convergence trends are indicated with the label $O(p_{ms})$ for the linear convergence and with $O(p_{ms}^2)$ for the quadratic one. As observed in Figure 4 and Figure 5, althought the transverse deflection is interpolated using quadratic shape functions, a quadratic and linear rate of convergence is exhibited for the errors defined in L^2 and H^1 norms, respectively, consistent with the behaviour observed in linear elements (as reported in Ref. [46]). The same rates of convergence

are found for each case of length-to-thickness ratios considered, e.g. a/h=10, 10^3 and 10^6, revealing the robustness of the adopted approach to address the transverse shear-locking problem.

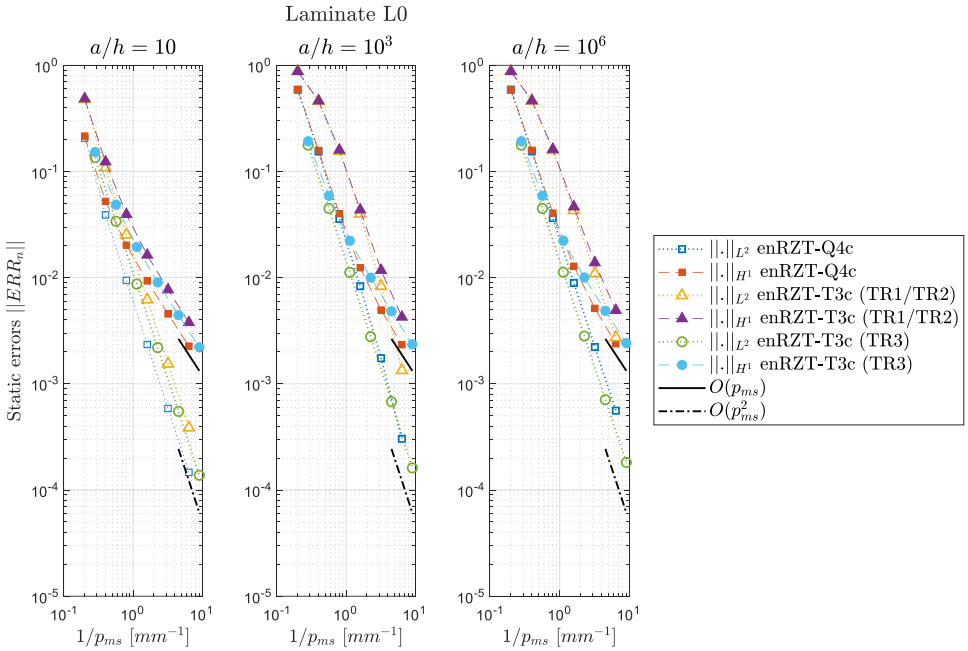

Figure 4: Estimated normalised errors in L^2 and H^1 norms (see Eqs. (37),(38)) for a cross-ply (L0) simply-supported square plate under bi-sinusoidal transverse pressure for different length-to-thickness ratios and mesh schemes.

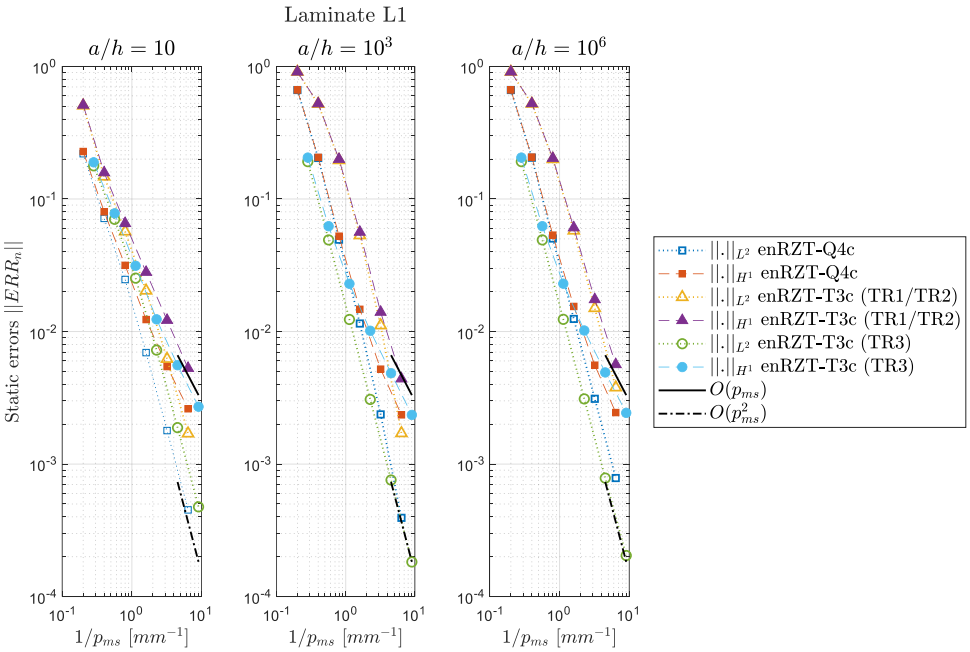

Figure 5: Estimated normalised errors in L^2 and H^1 norms (see Eqs. (37),(38)) for an antisymmetric angle-ply (L1) simply-supported square plate under bi-sinusoidal transverse pressure for different length-to-thickness ratios and mesh schemes.

In Figure 6 and Figure 7, the normalised errors on the fundamental frequency for simply-supported cross-ply (L0) and antisymmetric angle-ply (L2) plates are reported. Also for the modal case, the FE solution converges to the analytical one with a quadratic rate. Thus, the robustness of

the TRIA3 and QUAD4 elements in keeping the same convergence order is verified for different mesh configurations and length-to-thickness ratios.

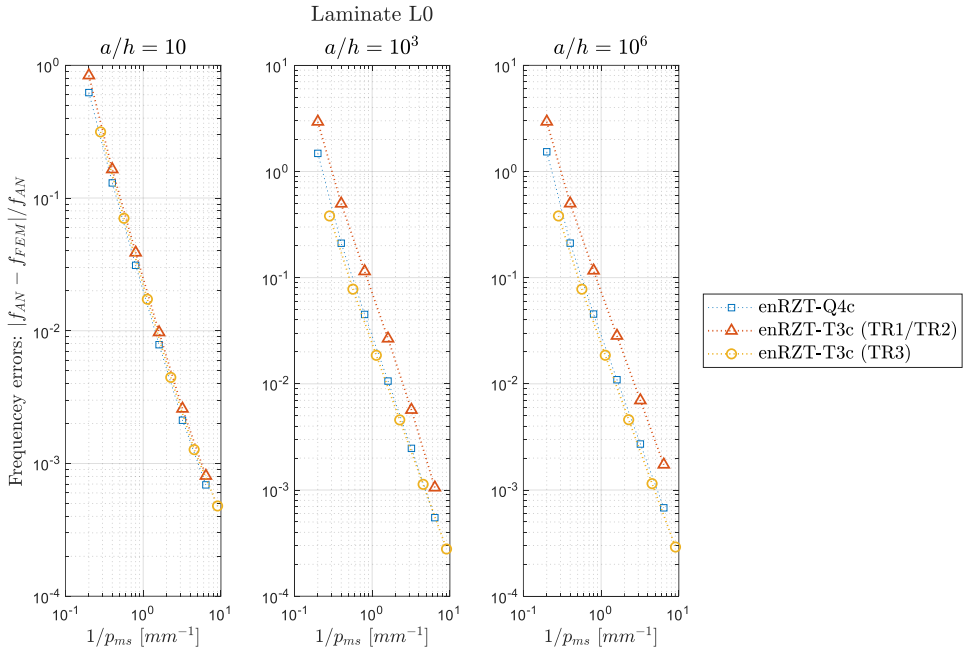

Figure 6: Normalised error on the fundamental frequency for a symmetric cross-ply (L0) simply-supported square plate for different length-to-thickness ratios and mesh schemes.

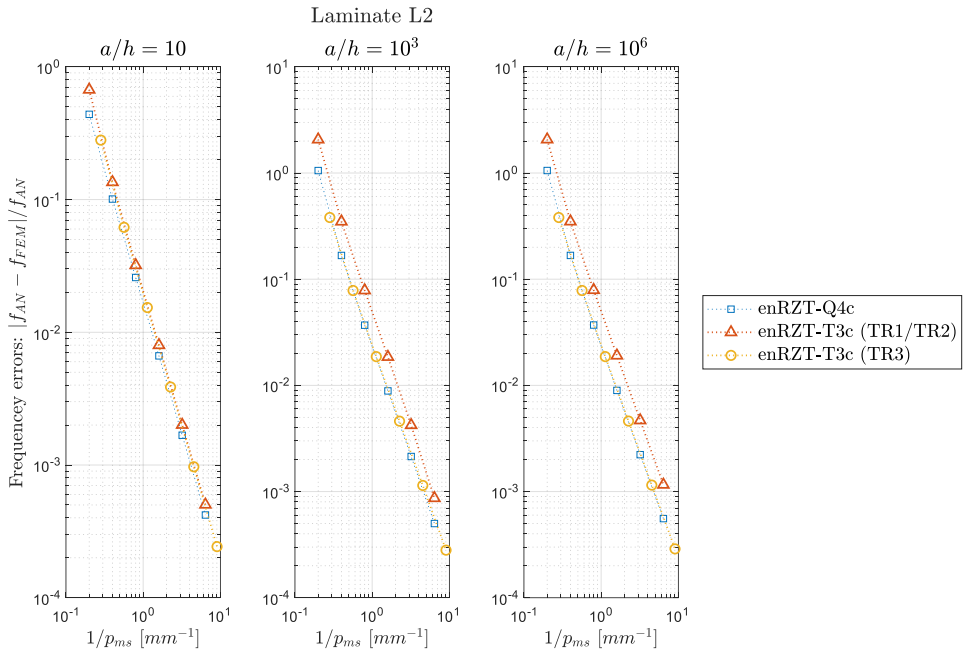

Figure 7: Normalised error on the fundamental frequency for an antisymmetric angle-ply (L0) simply-supported square plate for different length-to-thickness ratios and mesh schemes.

4.2. Mesh distortion and shear-locking influence

The effect of element distortion in mesh configuration and the influence of the shear-locking problem in maximum deflection and fundamental frequency predictions for simply-supported anti-symmetric angle-ply laminates are addressed here.

As highlighted in the convergence analysis, a 32x32 mesh discretisation is sufficient to reach the converged solution. Moreover, the TR3 structured mesh configuration is considered when enRZT-T3c elements are used. Figure 8 shows the quadrilateral and triangular mesh patterns for the distorted mesh configuration. According to the chosen notation, in this example the adopted 32x32 mesh discretisation means that even for distorted configuration, 32 elements are used along the x_1 direction and 32 are used along x_2 direction, as reported in Figure 8. The distortion criteria for a generic plate edge, as reported in Figure 8, assumes L_1 and L_2 as the lengths of the first and of the last element edges, respectively. Meanwhile, a linear variation has been adopted for the elements comprised within.

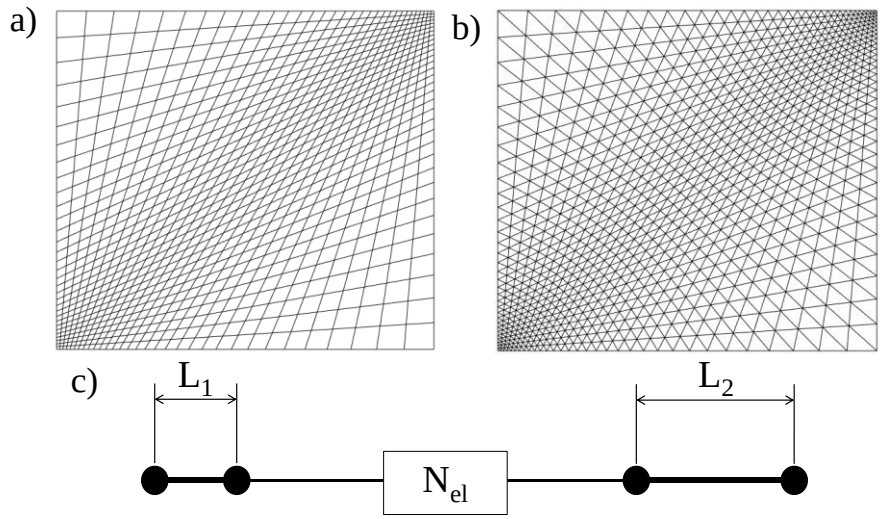

Figure 8: Distorted quadrilateral a) and triangular b) mesh discretisation (32x32); c) distortion criteria.

More specifically, for plate's edges with $x_1 = 0$ and $x_2 = 0$, $L_2 / L_1 = 10$, whereas for plate's edges with $x_1 = a$ and $x_2 = b$, $L_2 / L_1 = 0.1$.

For bending analysis, a bi-sinusoidal transverse pressure is considered, and according to the lamination scheme, simply-supported (SS-2) boundary conditions are adopted.

In Table 6 and Table 7, the percent errors for maximum central deflection and fundamental frequency computed using enRZT-T3c/enRZT-Q4c elements are reported for various plate length-to-thickness ratios. In addition, the analytical reference solution for static and free-vibration problems is provided in the first column of Table 6 and Table 7, respectively.

Table 6: Percent errors for maximum deflection $\bar{w}$ of simply-supported (SS-2) laminate L1 under bi-sinusoidal pressure. The reference dimensionless data are normalised according to Eq. (34).

en-RZT	***a/h***	**Regular mesh (32x32)**		**Distorted mesh (32x32)**	
		enRZT-Q4c	**enRZT-T3c**	**enRZT-Q4c**	**enRZT-T3c**
1.6054	*4*	0.025	-0.005	-0.303	-0.217
0.8721	*8*	-0.024	-0.037	-0.328	-0.238

0.7821	*10*	-0.037	-0.044	-0.332	-0.238
0.6926	*15*	-0.052	-0.052	-0.337	-0.238
0.6611	*20*	-0.058	-0.056	-0.340	-0.237
0.6270	*50*	-0.067	-0.061	-0.359	-0.236
0.6221	10^2	-0.072	-0.063	-0.418	-0.234
0.6205	10^3	-0.235	-0.074	-2.402	-0.190
0.6205	10^4	-0.307	-0.076	-3.196	-0.174
0.6205	10^5	-0.309	-0.076	-3.208	-0.174
0.6205	10^6	-0.309	-0.076	-3.208	-0.174

Table 7: Percent errors for fundamental frequency $\bar{f}$ of simply-supported (SS-2) laminate L2. The reference dimensionless data are normalised according to Eq. (34).

en-RZT	***a/h***	**Regular mesh (32x32)**		**Distorted mesh (32x32)**	
		enRZT-Q4c	**enRZT-T3c**	**enRZT-Q4c**	**enRZT-T3c**
1.470	*4*	0.155	0.084	0.286	0.190
2.072	*8*	0.165	0.094	0.312	0.228
2.208	*10*	0.168	0.097	0.320	0.238
2.376	*15*	0.171	0.101	0.329	0.251
2.445	*20*	0.173	0.102	0.334	0.257
2.527	*50*	0.175	0.104	0.345	0.266
2.539	10^2	0.177	0.106	0.362	0.275
2.543	10^3	0.214	0.114	0.688	0.336
2.543	10^4	0.240	0.132	0.781	0.358
2.543	10^5	0.240	0.132	0.782	0.358
2.543	10^6	0.240	0.132	0.782	0.358

The newly enRZT-Q4c and enRZT-T3c elements perform successfully for the entire range of length-to-thickness investigated (from very thick to ultra-thin regimes), with percent errors not higher than 0.4% in absolute value for regular mesh pattern and 3.21% for the distorted one. Clearly, higher differences between the reference solution (exact en-RZT) and the FEM one are expected when distorted mesh configurations are adopted since the numerical integration performs better with regular element geometry. In addition, the slightly higher errors observed in bending analysis can be attributed to the geometrical complexity of the distorted elements to follow the bi-sinusoidal load shape. In fact, for modal analysis, the errors for both enRZT-Q4c and enRZT-T3c elements are generally below the 1% for ultra-thin plates. The computed results confirm the effectiveness of the presented approach to solve the shear-locking issue. The adoption of the anisoparametric constrained strategy, effective in alleviating shear-locking up to $a/h=10^3$, along with the implementation of an appropriate ESC factor, extends the enRZT-Q4c and enRZT-T3c element suitability to ultra-thin structures. Moreover, the robustness and efficiency of both enRZT-Q4c and enRZT-T3c are clearly demonstrated, even in the presence of distorted mesh configurations.

4.3. Problem 1: fully clamped anti-symmetric angle-ply squared plate

In this Section, a new problem is addressed. A squared (*a/b*=1) anti-symmetric angle-ply plate with lamination scheme L3 is here considered. Each plate's edge of is clamped (C), and, for static analysis, a concentrated transverse force (F_0) is acting on the plate centre, at $(x_1, x_2) = (a/2, b/2)$. The length-to-thickness ratio (*a/h*) of the plate is 20 (moderately thick), with *a*=20 mm.

The reference result has been obtained by using a high-fidelity FE model with NASTRAN® HEXA20 solid elements. The 3D model of plate L3 is made up of 150 elements along both x_1 and x_2 directions, whereas 12 elements (3 for each layer) are used along thickness direction, for a total of 270000 solid elements and 3476775 dofs. The force applied in the 3D model is equally divided between the top and bottom central nodes to reduce the effect of transverse normal deformability not included in the en-RZT plate model. As for the en-RZT FEM solution, the plate is discretised using 50x50 elements in both plane directions, according to QD4 and TR3 regular mesh configuration, resulting in 18207 and 35707 total dofs for enRZT-Q4c and enRZT-T3c elements, respectively.

In this problem, for the normalised dimensionless quantities expressed using Eq. (34), $\bar{q}_0 = F_0/(ab)$ is considered, where the force intensity is $F_0 = -100N$.

Figure 9 compares the normalised transverse displacements of the clamped plate along the x_1 axis at $x_2=b/2$ considering the newly formulated en-RZT elements.

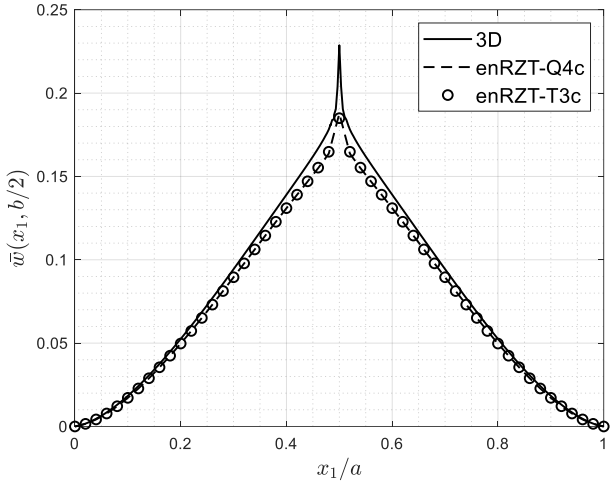

Figure 9: Normalised dimensionless transverse displacements (see, Eq. (34)) along x_1 axis at $x_2=b/2$ for laminate L3.

Since the 3D – NASTRAN® model includes the transverse normal deformability, the reference values reported in Figure 9 are mean values of the transverse displacement distribution along the thickness direction. Both enRZT-Q4c and enRZT-T3c elements accurately capture the

transverse displacements of a fully clamped plate with good accuracy with respect to the three-dimensional FE solution.

In Figure 10, the normalised through-the-thickness distributions of the in-plane displacements are displayed for the point located at $(x_1, x_2) = (a/5, b/2)$; in both NASTRAN® and en-RZT FE models, this corresponds to a nodal position. The en-RZT elements accurately predict the three-dimensional behaviour at an affordable computational cost for both in-plane displacement components. Moreover, the enRZT-Q4c and enRZT-T3c elements are capable to predict the effect of the shear coupling in the angle-ply lamination schemes, as shown in Figure 10. Despite the zigzag effect is not observable the through-the-thickness distribution of in-plane displacement in the x_1 direction, it is clearly present in the other direction, i.e. the x_2 one.

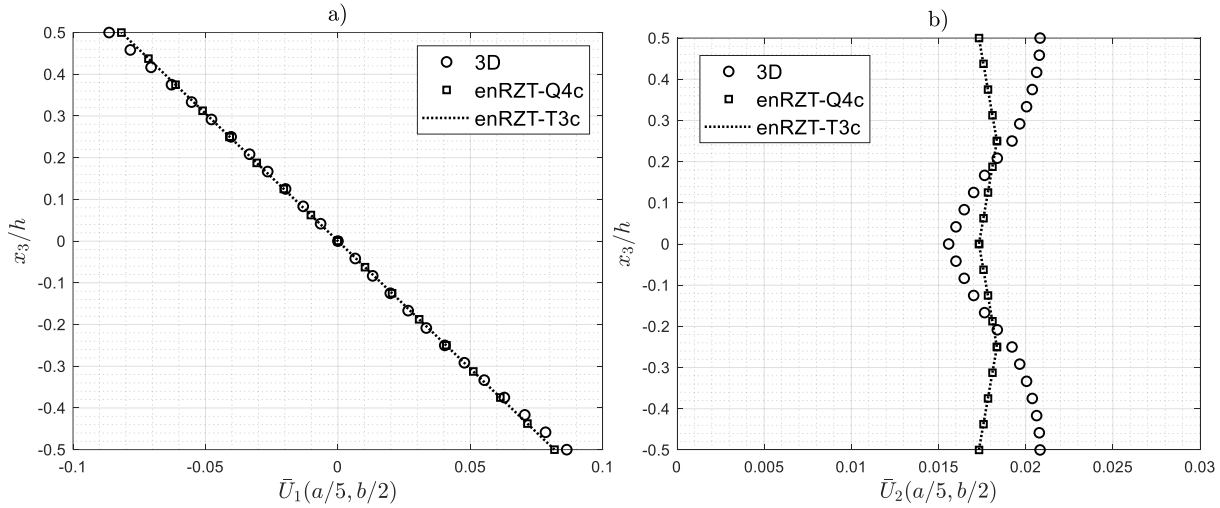

Figure 10: Normalised dimensionless through-the-thickness distributions of axial displacements at $(x_1, x_2) = (a/5, b/2)$ for laminate L3.

Table 8: Comparison of FE results with the 3D ones for in-plane strains ε_{11}, ε_{22} and γ_{12} (in $\mu m/m$) evaluated at $(a/20, 9b/20)$ point of laminate L3.

	x_3/h	3D	enRZT-Q4c	*err.* [%]	enRZT-T3c	*err.* [%]
ε_{11}	0.125	240.62	246.19	+2.31	246.11	+2.28
	0.375	787.03	784.65	-0.30	784.44	-0.33
ε_{22}	0.125	-43.28	-42.58	-1.63	-42.56	-1.68
	0.375	-109.55	-100.51	-8.24	-100.47	-8.28
γ_{12}	0.125	-157.39	-168.33	+6.95	-168.25	+6.90
	0.375	-93.02	-84.95	-8.68	-84.85	-8.79

Table 8 contains a comparison of the in-plane strains, i.e. ε_{11}, ε_{22} and γ_{12}, at different thickness coordinates for a point located at $(x_1, x_2) = (a/20, 9b/20)$. In both 3D NASTRAN® and enRZT-Q4c FE models, this point corresponds to the centroid of the elements, where the strain

quantities are evaluated. Using enRZT-T3c elements in TR3 configuration, the same point corresponds to a node shared by four elements. In this case the strains are obtained by averaging the four values computed at the centroid of the four triangular elements that share the common node. Minimal numerical differences are noticeable between enRZT-Q4c and enRZT-T3c elements. Despite the plate is moderately thick (for *a/h*=20, the transverse normal deformability is negligible but not null), the percent errors in the in-plane strains at the evaluated points and thickness coordinates do not exceed the 9%.

The dynamic behaviour of fully clamped laminate L3 has been investigated by computing its first ten normal modes and corresponding circular frequencies. Table 9 reports the normalised frequencies, according to Eq. (34), obtained using enRZT-Q4c and enRZT-T3c elements and the percent errors with respect to those obtained by the high-fidelity 3D - NASTRAN® model. Both the newly formulated elements are able to capture the fundamental frequency with an error not higher than 3.4%, and for higher modes with an error below the 8%.

Table 9: Normalised dimensionless natural frequencies $\overline{f}$ (see, Eq. (34)) and percent errors for the first ten transversal normal modes of fully clamped anti-symmetric angle-ply (L3) plate.

Mode n.	**3D**	**enRZT-Q4c**	***err.* [%]**	**enRZT-T3c**	***err.* [%]**
1	3.259	3.368	3.34	3.366	3.29
2	6.154	6.453	4.86	6.445	4.74
3	6.154	6.453	4.86	6.445	4.74
4	9.022	9.615	6.57	9.601	6.41
5	9.923	10.554	6.36	10.531	6.13
6	10.030	10.661	6.30	10.638	6.06
7	12.683	13.697	7.99	13.666	7.75
8	12.683	13.697	7.99	13.666	7.75
9	14.476	15.598	7.75	15.543	7.37
10	14.476	15.598	7.75	15.543	7.37

4.4. Problem 2: cantilever symmetric angle-ply rectangular plate

In this Section, the problem of a cantilever symmetrical laminated (L4) rectangular plate (*a/b*=3) is considered, with a length-to-thickness ratio considered *a/h = 15* (*a*=15 mm, moderately thick in x_1 direction) and a width-to-thickness ratio *b/h=5* (extremely thick in x_2 direction). For the static bending case, a uniform constant pressure of intensity $q_0 = -10\text{MPa}$ is acting on the reference plate surface, as reported in Figure 11.

The reference 3D model of plate L4, obtained using NASTRAN® solid (HEXA20) elements, adopted a discretisation with 180 elements and 60 along x_1 and x_2 directions, respectively; whereas 12 elements are considered along thickness direction, for a total of 129600 solid elements corresponding to 1679835 dofs. Also in this case, to reduce the effect of transverse

normal deformability, the pressure applied in the 3D FE model is equally divided between the top and bottom external surfaces.

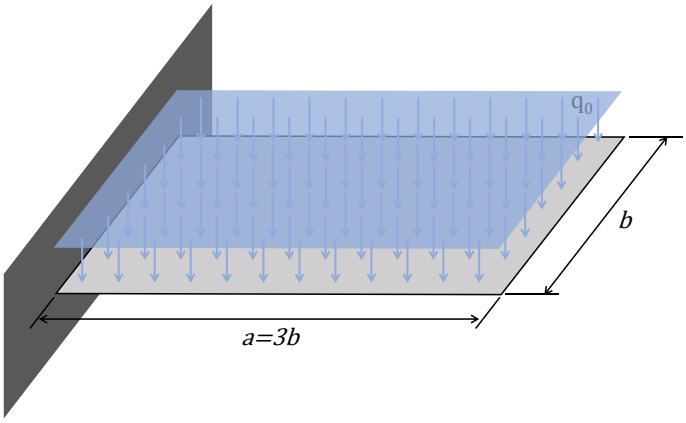

Figure 11: Cantilever rectangular plate under uniform applied pressure.

As for the en-RZT FEM solution, a discretisation of 60x20 elements in each direction is adopted according to QD4 and TR3 regular mesh configuration, resulting in 8967 and 17367 total dofs for enRZT-Q4c and enRZT-T3c element discretisations, respectively.

Table 10 reports a comparison between the FE en-RZT results and those coming from the high-fidelity 3D model. The point where the displacement quantities are evaluated corresponds to a node of the models. The point where the in-plane strains are evaluated, corresponds in both NASTRAN® and enRZT-Q4c models to the centroid of the elements. When using enRZT-T3c elements according to TR3 configuration, the point corresponds to a node shared by four triangular elements. As for the previous numerical problem, the strains are evaluated by averaging the values computed at the centroid of each of the four triangular elements that share the common node.

Table 10: Comparison of FE results with the 3D ones for displacements (given in mm) and in-plane strains (in $\mu m/m$) of laminate L4.

Point		x_3/h	**3D**	**enRZT-Q4c**	***err.* [%]**	**enRZT-T3c**	***err.* [%]**
$(a,0)$	U_1	0.5	0.8375	0.8094	-3.36	0.8116	-3.09
	U_2	0.5	-0.2956	-0.2813	-4.84	-0.2822	-4.53
	U_3	-	-19.47*	-18.78	-3.56	-18.84	-3.22
$\left(7a/120, 33b/40\right)$	ε_{11}	0.375	57379.9	55669.2	-2.98	55954.2	-2.48
	ε_{22}	0.375	-10677.2	-10065.9	-5.73	-10132.6	-5.10
	γ_{12}	0.375	-82356.1	-80250.7	-2.56	-80765.3	-1.93

* is a mean value of the thickness-wise 3D distribution.

Table 10 confirms the minimal numerical differences between enRZT-Q4c and enRZT-T3c elements in predicting both displacements and strains, with a percent errors below the 6%. A modal analysis has been performed to evaluate the dynamic behaviour of a cantilevered, symmetrical

laminated, angle-ply (L4) rectangular plate. In Table 11, the first seven normalised frequencies, according to Eq. (34), obtained using enRZT-Q4c and enRZT-T3c elements are reported and compared with those coming from the 3D - NASTRAN® model. Moreover, for each normal mode, Table 11 reports the percent errors between the en-RZT FE models and the 3D results.

Table 11: Normalised dimensionless natural frequencies $\bar{f}$ (see, Eq. (34)) and percent errors for the first seven transversal normal modes of cantilever rectangular symmetric angle-ply (L4) plate.

Mode n.	**3D**	**enRZT-Q4c**	***err.* [%]**	**enRZT-T3c**	***err.* [%]**
1	0.397	0.404	1.80	0.403	1.61
2	2.078	2.110	1.52	2.108	1.44
3	2.325	2.357	1.39	2.356	1.34
4	5.255	5.356	1.92	5.351	1.84
5	6.472	6.569	1.50	6.566	1.45
6	8.876	9.082	2.32	9.073	2.22
7	9.897	10.068	1.72	10.057	1.62

The predicting accuracy achieved by the en-RZT model through enRZT-Q4c and enRZT-T3c elements is remarkable, as highlighted by the errors reported in Table 11. The errors are lower than the 2.5% for the considered normal modes, with even lower values when enRZT-T3c elements are used, thanks to the TR3 mesh distribution adopted for this problem.

5. Conclusions

A three-node triangular and a four-node quadrilateral plate element based on the enhanced-Refined Zigzag Theory (en-RZT) have been developed to study general multilayered composite plates. Firstly, the recently developed en-RZT model is briefly recalled. The en-RZT displacement field is based only on seven kinematic unknowns, including three uniform displacements, two bending and two zigzag rotations. The enhanced zigzag functions are formulated so that the effect of coupling of transverse shear stresses for general lamination schemes is included at the in-plane local displacement level. Since the en-RZT requires only C^0-continuity of the shape functions, the finite element formulation with classical low-order isoparametric finite elements leads to the shear-locking issue.

In order to formulate robust and accurate triangular and quadrilateral finite elements based on the en-RZT, the anisoparametric constrained interpolation strategy has been adopted. Thanks to this interpolation approach, the full-quadrature integration can be adopted for stiffness, mass matrices and load vector computation to ensure variationally consistence and to reduce the occurrence of the energy zero modes due to the shear-locking issue. In addition, to enhance the robustness of the formulated elements and completely eliminate the locking problem, an appropriate Element Shear Correction (ESC) factor is derived through an energy approach. The

resulting triangular, enRZT-T3c, and quadrilateral, enRZT-Q4c, elements are free of locking even for ultra-thin plate regimes.

Static and dynamic assessments have been performed to evaluate the convergence behaviour of enRZT-T3c and enRZT-Q4c elements. When applied to cross-ply lamination schemes, the newly formulated elements guarantee the same results as the standard RZT, i.e. enRZT-Q4c element is equivalent to the ZTQ4c one. Furthermore, the robust convergence behaviour of both triangular and quadrilateral elements has been observed as quadratic in L^2-norm and linear in H^1-norm for various length-to-thickness ratios, ranging from thick to ultra-thin regimes, mesh and laminate configurations.

Moreover, the effect of mesh distortion has been addressed, and the elimination of the shear-locking from $a/h=4$ to $a/h=10^6$ has been demonstrated. Comparisons have been made with a set of new problems for which the analytical solution is not available, i.e. a fully clamped plate with a concentrated force and a cantilever rectangular plate with uniform load pressure. The results provided by both enRZT-T3c and enRZT-Q4c elements and compared with high-fidelity 3D FE models show a remarkable accuracy in predicting global quantities such as transverse displacements, natural frequencies and modal shapes, and local quantities, i.e. in-plane displacements and strains.

These novel elements offer an alternative and valid numerical tool for analysing more general laminated plates that exhibit a transverse anisotropy due to their stacking sequences while retaining their simplicity and low computational costs. Finally, the present elements can be considered as candidates for the application to shell laminated structures and more complex analysis, such as non-linear effects, transient responses and damage assessments.

Acknowledgments: Computational resources were provided by HPC@POLITO, a project of Academic Computing within the Department of Control and Computer Engineering at the Politecnico di Torino (http://www.hpc.polito.it).

Appendix A – Shape function definitions

In this Appendix, the expression of the shape functions that appear in Eq. (23).

For the quadrilateral elements, the bi-linear Lagrangian and bi-quadratic serendipity shape functions are defined in the natural coordinate system, i.e. $(\xi,\eta)\in[-1,+1]$:

$$
\begin{aligned}
&L_l(\xi,\eta)=\frac{1}{4}\left(1+\xi^{(l)}\xi\right)\left(1+\eta^{(l)}\eta\right) && (l=1\div 4)\\
&P_l(\xi,\eta)=\frac{1}{4}\left(1+\xi^{(l)}\xi\right)\left(1+\eta^{(l)}\eta\right)\left(\xi^{(l)}\xi+\eta^{(l)}\eta-1\right) && (l=1\div 4)\\
&P_{12}(\xi,\eta)=\frac{1}{2}\left(1-\xi^2\right)(1-\eta) \qquad P_{23}(\xi,\eta)=\frac{1}{2}\left(1-\eta^2\right)(1+\xi)\\
&P_{34}(\xi,\eta)=\frac{1}{2}\left(1-\xi^2\right)(1+\eta) \qquad P_{41}(\xi,\eta)=\frac{1}{2}\left(1-\eta^2\right)(1-\xi)
\end{aligned}
\tag{A.1}
$$

where, $\left(\xi^{(l)},\eta^{(l)}\right)$ are the natural coordinates of the corner node *l-th*.

For the triangular element, the area-coordinates are considered, i.e. (ξ_1,ξ_2). The expression for linear and quadratic shape functions follows:

$$
\begin{aligned}
&L_1=\xi_1; \qquad L_2=\xi_2; \qquad L_3=1-(\xi_1+\xi_2)\\
&P_l(\xi_1,\xi_2)=L_l(2L_l-1) \qquad (l=1,2,3)\\
&P_{lj}(\xi_1,\xi_2)=4L_lL_j \qquad \begin{pmatrix} l=1,2,3\\ j=2,3,1\end{pmatrix}
\end{aligned}
\tag{A.2}
$$

The remaining shape functions that appear in Eq. (26) are, for quadrilateral elements [40]

$$
\left.\begin{aligned}
S_{\theta_1}^{(l)}&=\frac{1}{8}\left[P_{kl}\left(x_{1l}-x_{1k}\right)+P_{lj}\left(x_{1l}-x_{1j}\right)\right]\\
S_{\theta_2}^{(l)}&=\frac{1}{8}\left[P_{kl}\left(x_{2l}-x_{2k}\right)+P_{lj}\left(x_{2l}-x_{2j}\right)\right]\\
S_{\psi_1}^{(l)}&=-S_{\theta_1}^{(l)}\\
S_{\psi_2}^{(l)}&=-S_{\theta_2}^{(l)}
\end{aligned}\right\}\begin{pmatrix} l=1,2,3,4\\ j=2,3,4,1\\ k=4,1,2,3\end{pmatrix}
\tag{A.3}
$$

and for triangular elements [39,40]

$$
\left.\begin{aligned}
S_{\theta_1}^{(l)}&=\frac{L_l}{2}\left[L_j\left(x_{1l}-x_{1k}\right)+L_k\left(x_{1l}-x_{1j}\right)\right]\\
S_{\theta_2}^{(l)}&=\frac{L_l}{2}\left[L_j\left(x_{2l}-x_{2k}\right)+L_k\left(x_{2l}-x_{2j}\right)\right]\\
S_{\psi_1}^{(l)}&=-S_{\theta_1}^{(l)}\\
S_{\psi_2}^{(l)}&=-S_{\theta_2}^{(l)}
\end{aligned}\right\}\begin{pmatrix} l=1,2,3\\ j=2,3,1\\ k=3,1,2\end{pmatrix}
\tag{A.4}
$$

where $\left(x_{1l},x_{2l}\right)$ are the global coordinates for the node *l*-th.

Appendix B – Elemental strain matrices definition

The full expressions of the matrices that contain the derivatives of the shape functions as reported in Eq. (28) are:

$$
\mathbb{B}_{mi}=\begin{bmatrix}
L_{i,1} & 0 & 0 & 0 & 0 & 0 & 0\\
0 & L_{i,2} & 0 & 0 & 0 & 0 & 0\\
L_{i,2} & L_{i,1} & 0 & 0 & 0 & 0 & 0
\end{bmatrix}
\tag{B.1}
$$

$$\mathbb{B}_{\theta i}=\begin{bmatrix}\mathbf{0} & \hat{\mathbb{B}}_{\theta_i}\end{bmatrix};\ \mathbb{B}_{\psi i}=\begin{bmatrix}\mathbf{0} & \hat{\mathbb{B}}_{\psi_i}\end{bmatrix};\ \mathbb{B}_{si}=\begin{bmatrix}\hat{\mathbb{B}}_{w_i} & \hat{\mathbb{B}}_{s_i}\end{bmatrix} \tag{B.2}$$

with

$$\hat{\mathbb{B}}_{\theta_i}=\begin{bmatrix}L_{i,1} & 0 & 0 & 0\\ 0 & L_{i,2} & 0 & 0\\ L_{i,2} & L_{i,1} & 0 & 0\end{bmatrix};\ \hat{\mathbb{B}}_{\psi_i}=\begin{bmatrix}0 & 0 & L_{i,1} & 0\\ 0 & 0 & 0 & L_{i,2}\\ 0 & 0 & L_{i,2} & 0\\ 0 & 0 & 0 & L_{i,1}\end{bmatrix} \tag{B.3}$$

and

$$\hat{\mathbb{B}}_{w_i}=\begin{bmatrix}0 & 0 & L_{i,1}\\ 0 & 0 & L_{i,2}\\ 0 & 0 & 0\\ 0 & 0 & 0\end{bmatrix};\ \hat{\mathbb{B}}_{s_i}=\begin{bmatrix}L_i+S^{(i)}_{\theta 1,1} & S^{(i)}_{\theta 2,1} & S^{(i)}_{\psi 1,1} & S^{(i)}_{\psi 2,1}\\ S^{(i)}_{\theta 1,2} & L_i+S^{(i)}_{\theta 2,2} & S^{(i)}_{\psi 1,2} & S^{(i)}_{\psi 2,2}\\ 0 & 0 & L_i & 0\\ 0 & 0 & 0 & L_i\end{bmatrix} \tag{B.4}$$

Moreover, the bending and transverse shear stiffness matrices, i.e. $\mathbf{K}_b^{(e)}$ and $\mathbf{K}_s^{(e)}$, in Eq. (33) that are associated with the bending and zigzag rotations degrees of freedom, are expressed as follows:

$$\mathbf{K}_b^{(e)}\left(\theta_1,\theta_2,\psi_1,\psi_2\right)=\int_{\Omega^{(e)}}\begin{bmatrix}\mathbf{B}_\theta\\ \mathbf{B}_\psi\end{bmatrix}^T\begin{bmatrix}\mathbf{D} & \mathbf{B}^\phi\\ \mathbf{B}^{\phi T} & \mathbf{D}^\phi\end{bmatrix}\begin{bmatrix}\mathbf{B}_\theta\\ \mathbf{B}_\psi\end{bmatrix}d\Omega \tag{B.5}$$

$$\mathbf{K}_s^{(e)}\left(\theta_1,\theta_2,\psi_1,\psi_2\right)=\int_{\Omega^{(e)}}\mathbf{B}_s{}^T\begin{bmatrix}\mathbf{A}_t & \mathbf{B}_t\\ \mathbf{B}_t{}^T & \mathbf{D}_t\end{bmatrix}\mathbf{B}_s d\Omega \tag{B.6}$$

where

$$\mathbf{B}_\theta=\begin{bmatrix}\hat{\mathbb{B}}_{\theta_i}\end{bmatrix},\ \mathbf{B}_\psi=\begin{bmatrix}\hat{\mathbb{B}}_{\psi_i}\end{bmatrix},\ \mathbf{B}_s=\begin{bmatrix}\hat{\mathbb{B}}_{s_i}\end{bmatrix}\ \begin{cases}\left(i=1\div 3\right)\text{ for TRIA3}\\ \left(i=1\div 4\right)\text{ for QUAD4}\end{cases} \tag{B.7}$$

References

1. N. J. Pagano, "Exact Solutions for Rectangular Bidirectional Composites and Sandwich Plates," J. Compos. Mater., **4**, No. 1, 20-34 (1970). https://doi.org/10.1177/002199837000400102.
2. A. K. Noor and W. S. Burton, "Three-Dimensional Solutions for Antisymmetrically Laminated Anisotropic Plates," J. Appl. Mech., **57**, No. 1, 182-188 (1990). https://doi.org/10.1115/1.2888300.
3. M. Savoia and J. N. Reddy, "A Variational Approach to Three-Dimensional Elasticity Solutions of Laminated Composite Plates," J. Appl. Mech., **59**, No. 2S, S166-S175 (1992). https://doi.org/10.1115/1.2899483.
4. S. Abrate and M. Di Sciuva, "Equivalent single layer theories for composite and sandwich structures: A review," Compos. Struct., **179**, 482-494 (2017). https://doi.org/10.1016/j.compstruct.2017.07.090.

5. S. Abrate and M. Di Sciuva, in: P. W. R. Beaumont and C. H. Zweben (eds.), Comprehensive Composite Materials II, Ch 1.16, Elsevier (2018), pp. 399-425.
6. K. M. Liew, Z. Z. Pan, and L. W. Zhang, "An overview of layerwise theories for composite laminates and structures: Development, numerical implementation and application," Compos. Struct., **216**, 240-259 (2019). https://doi.org/10.1016/j.compstruct.2019.02.074.
7. M. Di Sciuva, "Development of an anisotropic, multilayered, shear-deformable rectangular plate element," Comput. Struct., **21**, No. 4, 789-796 (1985). https://doi.org/10.1016/0045-7949(85)90155-5.
8. M. Cho and R. Parmerter, "Efficient higher order composite plate theory for general lamination configurations," AIAA J., **31**, No. 7, 1299-1306 (1993). https://doi.org/10.2514/3.11767.
9. U. Icardi, "A three-dimensional zig-zag theory for analysis of thick laminated beams," Compos. Struct., **52**, No. 1, 123-135 (2001). https://doi.org/10.1016/S0263-8223(00)00189-6.
10. R. C. Averill, "Static and dynamic response of moderately thick laminated beams with damage," Compos. Eng., **4**, No. 4, 381-395 (1994). https://doi.org/10.1016/S0961-9526(09)80013-0.
11. H. Murakami, "Laminated Composite Plate Theory With Improved In-Plane Responses," J. Appl. Mech, **53**, No. 3, 661-666 (1986). https://doi.org/10.1115/1.3171828.
12. A. Tessler, M. Di Sciuva, and M. Gherlone, "Refinement of Timoshenko Beam Theory for Composite and Sandwich Beams using Zigzag Kinematics," NASA/TP-2007-215086, 1-45 (2007).
13. A. Tessler, M. Di Sciuva, and M. Gherlone, "Refined Zigzag Theory for Laminated Composite and Sandwich Plates," NASA/TP-2009-215561, 1-53 (2009).
14. M. Gherlone, A. Tessler, and M. Di Sciuva, "C^0 beam elements based on the Refined Zigzag Theory for multilayered composite and sandwich laminates," Compos. Struct., **93**, No. 11, 2882-2894 (2011). https://doi.org/10.1016/j.compstruct.2011.05.015.
15. E. Oñate, A. Eijo, and S. Oller, "Simple and accurate two-noded beam element for composite laminated beams using a refined zigzag theory," Comput. Methods Appl. Mech. Eng., **213-216**, 362–382 (2012). https://doi.org/10.1016/j.cma.2011.11.023.
16. H. Wimmer, W. Hochhauser, and K. Nachbagauer, "Refined Zigzag Theory: an appropriate tool for the analysis of CLT-plates and other shear-elastic timber structures," Eur. J. Wood Prod., **78**, No. 6, 1125–1135 (2020). https://doi.org/10.1007/s00107-020-01586-x.
17. A. Eijo, E. Oñate, and S. Oller, "A four-noded quadrilateral element for composite laminated plates/shells using the refined zigzag theory," Int. J. Numer. Meth. Eng., **95**, No. 8, 631–660 (2013). https://doi.org/10.1002/nme.4503.

18. L. Iurlaro, M. Gherlone, M. Di Sciuva, and A. Tessler, “Assessment of the Refined Zigzag Theory for bending, vibration, and buckling of sandwich plates: a comparative study of different theories,” Compos. Struct., **106**, 777–792 (2013). https://doi.org/10.1016/j.compstruct.2013.07.019.
19. D. Versino, M. Gherlone, and M. Di Sciuva, “Four-node shell element for doubly curved multilayered composites based on the Refined Zigzag Theory,” Compos. Struct., **118**, 392–402 (2014). https://doi.org/10.1016/j.compstruct.2014.08.018.
20. L. Iurlaro, M. Gherlone, and M. Di Sciuva, “Bending and free vibration analysis of functionally graded sandwich plates using the Refined Zigzag Theory,” J. Sandw. Struct. Mater., **16**, No. 6, 669–699 (2014). https://doi.org/10.1177/1099636214548618.
21. M. Dorduncu, “Flexure Analysis of Functionally Graded Plates Using {2,2}-Refined Zigzag Theory,” JAST, **12**, No. 1, 19–30 (2019).
22. M. Dorduncu, “Stress analysis of sandwich plates with functionally graded cores using peridynamic differential operator and refined zigzag theory,” Thin-Walled Struct., **146**, 106468 (2020). https://doi.org/10.1016/j.tws.2019.106468.
23. R. M. Groh, P. M. Weaver, and A. Tessler, “Application of the Refined Zigzag Theory to the Modeling of Delaminations in Laminated Composites,” NASA/TM-2015-218808, 1-22 (2015).
24. R. M. J. Groh and P. M. Weaver, “On displacement-based and mixed-variational equivalent single layer theories for modelling highly heterogeneous laminated beams,” Int. J. Solids Struct., **59**, 147-170 (2015). https://doi.org/10.1016/j.ijsolstr.2015.01.020.
25. M. Patni, S. Minera, R. Groh, P. Weaver, and A. Pirrera, “Efficient 3D Stress Capture of Variable Stiffness and Sandwich Beam Structures,” in: AIAA Scitech Forum (2019). https://doi.org/10.2514/6.2019-1763.
26. L. G. Nallim, S. Oller, E. Oñate, and F. G. Flores, “A hierarchical finite element for composite laminated beams using a refined zigzag theory,” Compos. Struct., **163**, 168-184 (2017). https://doi.org/10.1016/j.compstruct.2016.12.031.
27. F. G. Flores, S. Oller, and L. G. Nallim, “On the analysis of non-homogeneous laminates using the refined zigzag theory,” Compos. Struct., **204**, 791-802 (2018). https://doi.org/10.1016/j.compstruct.2018.08.018.
28. A. Ascione and M. Gherlone, “Nonlinear static response analysis of sandwich beams using the Refined Zigzag Theory,” J. Sandw. Struct. Mater., **22**, No. 7, 2550-2286 (2018). https://doi.org/10.1177/1099636218795381.

29. A. Ascione, M. Gherlone, and A. C. Orifici, “Nonlinear static analysis of composite beams with piezoelectric actuator patches using the Refined Zigzag Theory,” Compos. Struct., **282**, 115018 (2022). https://doi.org/10.1016/j.compstruct.2021.115018.
30. K. A. Hasim, “Isogeometric static analysis of laminated composite plane beams by using refined zigzag theory,” Compos. Struct., **186**, 365-374 (2018). https://doi.org/10.1016/j.compstruct.2017.12.033.
31. K. A. Hasim, A. Kefal, and E. Madenci, “Isogeometric plate element for unstiffened and blade stiffened laminates based on refined zigzag theory,” Compos. Struct., **222**, 110931 (2019). https://doi.org/10.1016/j.compstruct.2019.110931.
32. K. A. Hasim and A. Kefal, “Isogeometric static analysis of laminated plates with curvilinear fibers based on Refined Zigzag Theory,” Compos. Struct., **256**, 113097 (2021). https://doi.org/10.1016/j.compstruct.2020.113097.
33. L. Iurlaro, M. Gherlone, M. Di Sciuva, and A. Tessler, “Refined Zigzag Theory for laminated composite and sandwich plates derived from Reissner’s Mixed Variational Theorem,” Compos. Struct., **133**, 809-817 (2015). https://doi.org/10.1016/j.compstruct.2015.08.004.
34. A. Tessler, “Refined zigzag theory for homogeneous, laminated composite, and sandwich beams derived from Reissner’s mixed variational principle,” Meccanica, **50**, No. 10, 2621-2648 (2015). https://doi.org/10.1007/s11012-015-0222-0.
35. M. Gherlone, “Tria and quad plate finite elements based on $RZT^{(m)}$ for the analysis of multilayered sandwich structures,” Compos. Struct., **220**, 510-520 (2019). https://doi.org/10.1016/j.compstruct.2019.04.032.
36. A. Kefal, K. A. Hasim, and M. Yildiz, “A novel isogeometric beam element based on mixed form of refined zigzag theory for thick sandwich and multilayered composite beams,” Compos. B Eng., **167**, 100-121 (2019). https://doi.org/10.1016/j.compositesb.2018.11.102.
37. A. Kutlu, M. Dorduncu, and T. Rabczuk, “A novel mixed finite element formulation based on the refined zigzag theory for the stress analysis of laminated composite plates,” Compos. Struct., **267**, 113886 (2021). https://doi.org/10.1016/j.compstruct.2021.113886.
38. M. Di Sciuva, M. Gherlone, L. Iurlaro, and A. Tessler, “A class of higher-order C^0 composite and sandwich beam elements based on the Refined Zigzag Theory,” Compos. Struct., **132**, 784-803 (2015). https://doi.org/10.1016/j.compstruct.2015.06.071.
39. D. Versino, M. Gherlone, M. C. Mattone, M. Di Sciuva, and A. Tessler, “C^0 triangular elements based on the Refined Zigzag Theory for multilayered composite and sandwich plates,” Compos. B Eng., **44**, No. 1, 218-230 (2013). https://doi.org/10.1016/j.compositesb.2012.05.026.

40. M. Gherlone, D. Versino, and V. Zarra, “Multilayered triangular and quadrilateral flat shell elements based on the Refined Zigzag Theory,” Compos. Struct., 111629 (2019). https://doi.org/10.1016/j.compstruct.2019.111629.
41. M. Di Sciuva and M. Sorrenti, “A Family of C^0 Quadrilateral Plate Elements Based on the Refined Zigzag Theory for the Analysis of Thin and Thick Laminated Composite and Sandwich Plates,” J. Compos. Science, **3**, No. 4, 1-30 (2019). https://doi.org/10.3390/jcs3040100.
42. H. Wimmer and C. Celigoj, “An edge-based smoothed three-node composite plate element with refined zigzag kinematics,” Compos. Struct., **274**, 114204 (2021). https://doi.org/10.1016/j.compstruct.2021.114204.
43. P. Zoghipour, K. A. Hasim, A. Kefal, and M. Yildiz, “Implementation of shear-locking-free triangular refined zigzag element for structural analysis of multilayered plates with curvilinear fibers,” Compos. Struct., **305**, 116462 (2023). https://doi.org/10.1016/j.compstruct.2022.116462.
44. F. G. Flores, “Implementation of the refined zigzag theory in shell elements with large displacements and rotations,” Compos. Struct., **118**, 560-570 (2014). https://doi.org/10.1016/j.compstruct.2014.07.034.
45. E. Oñate, Structural Analysis with the Finite Element Method. Linear Statics: Volume 2: Beams, Plates and Shells, Springer Science+Business Media B.V., Netherlands (2013). https://doi.org/10.1007/978-1-4020-8743-1
46. K.-J. Bathe, Finite Element Procedures, 2nd edition, Prentice-Hall, Pearson Education, Inc., Englewood Cliffs, N.J. (1996).
47. T. J. R. Hughes, M. Cohen, and M. Haroun, “Reduced and selective integration techniques in the finite element analysis of plates,” Nucl. Eng. Des., **46**, No. 1, 203-222 (1978). https://doi.org/10.1016/0029-5493(78)90184-X.
48. E. Oñate, O. C. Zienkiewicz, B. Suarez, and R. L. Taylor, “A general methodology for deriving shear constrained Reissner-Mindlin plate elements,” Int. J. Num. Meth. Eng., **33**, No. 2, 345-367 (1992). https://doi.org/10.1002/nme.1620330208.
49. S. S. Murthy and R. H. Gallagher, “A triangular thin-shell finite element based on discrete Kirchhoff theory,” Comput. Methods Appl. Mech. Eng., **54**, No. 2, 197–222 (1986). https://doi.org/10.1016/0045-7825(86)90126-X.
50. I. Katili, “A new discrete Kirchhoff-Mindlin element based on Mindlin-Reissner plate theory and assumed shear strain fields—part I: An extended DKT element for thick-plate bending analysis,” Int. J. Num. Meth. Eng., **36**, No. 11, 1859–1883 (1993). https://doi.org/10.1002/nme.1620361106.

51. K.-U. Bletzinger, M. Bischoff, and E. Ramm, “A unified approach for shear-locking-free triangular and rectangular shell finite elements,” Comput. Struct., **75**, No. 3, 321–334 (2000). https://doi.org/10.1016/S0045-7949(99)00140-6.
52. K. J. Bathe and F. Brezzi, “On the convergence of a four-node plate bending element based on Mindlin–Reissner plate theory and a mixed interpolation,” in Proc. Mathematics of Finite Elements and Applications V (1985), pp. 491-503. https://doi.org/10.1016/B978-0-12-747255-3.50042-3.
53. K.-J. Bathe, M. L. Bucalem, and F. Brezzi, “Displacement and stress convergence of our MITC plate bending elements,” Eng. Comput., **7**, No. 4, 291-302 (1990). https://doi.org/10.1108/eb023816.
54. A. Tessler and S. B. Dong, “On a hierarchy of conforming Timoshenko beam elements,” Comput. Struct., **14**, No. 3, 335-344 (1981). https://doi.org/10.1016/0045-7949(81)90017-1.
55. A. Tessler and T. J. R. Hughes, “An improved treatment of transverse shear in the Mindlin-type four-node quadrilateral element,” Comput. Methods Appl. Mech. Eng., **39**, No. 3, 311-335 (1983). https://doi.org/10.1016/0045-7825(83)90096-8.
56. A. Tessler and T. J. R. Hughes, “A three-node Mindlin plate element with improved transverse shear,” Comput. Methods Appl. Mech. Eng., **50**, No. 1, 71-101 (1985). https://doi.org/10.1016/0045-7825(85)90114-8.
57. M. Sorrenti, M. Di Sciuva, and A. Tessler, “A robust four-node quadrilateral element for laminated composite and sandwich plates based on Refined Zigzag Theory,” Comput. Struct., **242**, 106369 (2021). https://doi.org/10.1016/j.compstruc.2020.106369.
58. M. Sorrenti and M. Di Sciuva, “An Enhancement of the Warping Shear Functions of Refined Zigzag Theory,” J. Appl. Mech., **88**, No. 084501, (2021). https://doi.org/10.1115/1.4050908.
59. I. Kreja and A. Sabik, “Equivalent single-layer models in deformation analysis of laminated multilayered plates,” Acta Mech., **230**, No. 8, 2827–2851 (2019). https://doi.org/10.1007/s00707-019-02434-7.
60. M. Sorrenti, M. Gherlone, and M. Di Sciuva, “Buckling analysis of angle-ply multilayered and sandwich plates using the enhanced Refined Zigzag Theory,” P. Est. Acad. Sci., **71**, No. 1, 84-102 (2022). https://doi.org/10.3176/proc.2022.1.08.
61. M. Sorrenti, M. Gherlone, and M. D. Sciuva, “Free vibration analysis of angle-ply laminated and sandwich plates using enhanced refined zigzag theory,” in: AIP Conference Proceedings ICNAAM2021, **2849**, No. 1, (2023). https://doi.org/10.1063/5.0162538.

62. M. Sorrenti, Refined Zigzag Models for the Response of General Multilayered Composite and Sandwich Structures: Numerical and Experimental Investigations, Politecnico di Torino, Torino (2023).